

Summary of Doctoral Thesis

# Halil Arslan

MECHANISM OF PHOTOCHROMISM IN YTTRIUM OXYHYDRIDE AND GROWTH KINETICS OF YTTRIUM OXIDE THIN FILMS



# FACULTY OF SCIENCE AND TECHNOLOGY

# Halil Arslan

# MECHANISM OF PHOTOCHROMISM IN YTTRIUM OXYHYDRIDE AND GROWTH KINETICS OF YTTRIUM OXIDE THIN FILMS

SUMMARY OF DOCTORAL THESIS

Submitted for the doctoral degree in Physics and Astronomy Subfield of Solid State Physics The doctoral thesis was carried out at the institute of Institute of Solid State Physics, the epartment of Physics, Astronomy; Faculty of Science and Technology, the University of Latvia from 2018 to 2025.









The thesis contains the introduction, seven chapters, thesis, reference list, and appendices.

Form of the thesis: dissertation in Physics, Astronomy, and Mechanics, Subfield of Solid state physics.

#### **Thesis Supervisors**

- Juris Purāns, Dr. habil. phys., Institute of Solid State Physics, University of Latvia, Latvia:
- 2. Smagul Karazhanov, Dr. habil. phys.; Institute for Energy Technology, Norway, Institute of Solid State Physics, University of Latvia, Latvia.

#### Thesis Reviewers

- 1. Aline Rougier, Dr.; University of Bordeaux, CNRS, Bordeaux INP, ICMCB, France:
- Lars Österlund, Professor; Department of Materials Science and Engineering, Uppsala University, Sweden;
- Andris Anspoks, Dr. phys.; Institute of Solid State Physics, University of Latvia, Latvia.

This doctoral thesis will be defended in a public session of the Promotional Committee of the Faculty of Science and Technology, University of Latvia, on April 25, 2025, at the Institute of Solid State Physics, Kengaraga Street 8.

The thesis is available at the Library of the University of Latvia (Raina Blvd 19, Riga).

#### **Chairman of the Doctoral Committee:**

Linards Skuja, Dr. habil. phys.

Leading researcher of the Institute of Solid State Physics, University of Latvia

#### **Secretary of the Promotional Committee:**

Sintija Siliņa

© University of Latvia, 2025

© Halil Arslan, 2025

ISBN 978-9934-36-367-2 ISBN 978-9934-36-368-9 (PDF)

# **Abstract**

Yttrium, a rare-earth metal, plays a vital role in advanced technologies such as fusion reactors<sup>1</sup>, superconductors<sup>2</sup>, and smart windows<sup>3</sup> due to its versatile chemistry. Yttrium compounds can form either single- or multi-anion systems, with yttrium monoxide (YO), where Y has a 2+ oxidation state (an unusual state for yttrium), representing a single-anion system that exhibits semiconducting properties<sup>4</sup>, while yttrium oxyhydride (YHO), as a double-anion system, is known for its unique photochromic behavior under ambient conditions, making it particularly relevant for smart window applications<sup>3</sup>.

Despite over a decade of research by multiple groups and efforts toward commercialization, including the production of windows, the mechanism behind the photochromic effect of YHO remains unclear. This gap in understanding hinders advancements in addressing degradation, enhancing photochromic performance, controlling color, increasing durability, and fully utilizing the material's potential applications. In this work, we studied YHO thin films produced by e-beam and reactive magnetron sputtering using various methods, including X-ray absorption spectroscopy (XAS), spectroscopic ellipsometry, X-ray diffraction (XRD), and ion beam instruments, combined with reverse Monte Carlo (RMC) simulations and ab initio multiple-scattering calculations. We report a breakthrough in understanding the mechanism behind the photochromic effect in YHO, rooted in the kinetics of anionic vacancies and the previously observed light-induced lattice relaxation, which enhances our knowledge of its material properties.

In addition, our findings indicate that during thin film growth, yttrium/yttrium oxide thin films undergo a metal--insulator transition as oxygen partial pressure increases, accompanied by distinct structural transformations (crystalline--amorphous-crystalline) at room temperature. At the same oxygen partial pressure level in the amorphous region, higher deposition temperatures ( $\sim$ 623 K) promote the formation of yttrium monoxide (YO) with yttrium in the 2+ oxidation state alongside Y<sub>2</sub>O<sub>3</sub>, resulting in a semi-transparent, semiconducting material.

# **Contents**

L.	IST OF	ABBREVIATIONS	6
1	INT	RODUCTION	7
	1.1	Literature Overview	7
	1.2	Objective of the Thesis	8
	1.3	Scientific Novelty	9
	1.4	Author's Contribution	10
2	MET	THODOLOGY	12
3	RES	ULTS AND DISCUSSIONS	14
	3.1	Yttrium/Yttrium Oxide Thin Films	14
	3.1.1	Structural Characterization	14
	3.1.2	2 Electrical Characterization	17
	3.1.3	3 Chemical Characterization	18
	3.1.4	4 Optical Characterization	20
	3.2	Photochromic Yttrium Oxyhydride Thin Films	23
	3.2.1	Structural and Morphological Characterization	23
	3.2.2	2 Chemical Characterization	25
	3.2.3	Optical Characterization	27
	3.2.4	Chemical and Structural Characterization	30
	3.3	Temperature-Dependent Structural Variation in Photoch	romic
	Yttriun	n Oxyhydride	32
	3.3.1	Optical Characterization	32
	3.3.2	2 Structural Characterization	32
	3.3.3	Radial Distribution Function Analysis	34

3.4	Role	e of Anion Vacancies and Lattice Dynamics in Photochromic	2
Yttri	ium Oxyhy	dride3	7
	3.4.1	Optical and Nanoscale Structural Characterization 3	7
	3.4.2	Light-Induced Chemical and Structural Characterization. 3	8
	3.4.3	Relationship Between Atomic-Scale and Nanoscale	
	Structural	Variations4	0
	3.4.4	Electronic Structure and Optical Characterization 4	0
4	SUMMA	RY AND CONCLUSION4	2
Mai	n Theses	4	5
Autl	nors' Paten	t and Publication List4	6
Parti	icipation in	Conferences	7
Parti	icipation in	International Schools	8
Parti	icipation in	Large-Scale Research Infrastructure-Based Experiments 4	9
Bibl	iography	5	0

# LIST OF ABBREVIATIONS

UV-VIS	Ultraviolet-Visible Spectroscopy
SE	Spectroscopic Ellipsometry
trSE	Time-resolved Spectroscopic Ellipsometry
<b>MSE</b>	Mean Squared Error
DO	Drude oscillator
GO	Gaussian oscillator
TLO	Tauc-Lorentz oscillator
HJPS	Herzinger-Johs parameterized semiconductor
XRD	X-ray Diffraction
trXRD	Time-resolved X-ray Diffraction
FCC	Face centered cubic
XPS	X-ray Photoelectron Spectroscopy
UPS	Ultraviolet Photoelectron Spectroscopy
SEM	Scanning Electron Microscopy
TEM	Transmission Electron Microscopy
SIMS	Secondary-ion Mass Spectrometry
TDCm	Temperature Dependent Conductivity Measurements
XAS	X-ray Absorption Spectroscopy
XANES	X-ray Absorption Near Edge Structure
<b>EXAFS</b>	Extended X-ray Absorption Fine Structure
FT	Fourier Transform
<i>RMC</i>	Reverse Monte Carlo
RDFs	Radial Distribution Functions
DFT	Density Functional Theory
RBS	Rutherford Backscattering Spectrometry
TOF-E ERDA	Time-of-Flight Elastic Recoil Detection Analysis
DC	Direct-Current
HiPIMS	High-power Impulse Magnetron Sputtering

# 1 INTRODUCTION

#### 1.1 Literature Overview

Yttrium oxyhydride (YHO) belongs to the emerging class of materials called mixed anion systems that include more than one type of anion. Such material might possess unique properties that are not available in single anion counterparts. As discovered by Mongstad et. al. YHO, exhibits photochromic properties at room temperature<sup>3</sup>. Upon illumination with sunlight, the material absorbs the UV light and changes its color from the transparent state with transmittance T>85% to the Photodarkened state with T<30%.

Unlike conventional inorganic oxide-based chromic films that require heating or an electric field for bleaching, YHO offers both photodarkening and bleaching under ambient conditions without the need for additional energy input. Furthermore, the limited lifespan of polymer-based photochromic materials, often containing hazardous chemicals, restricts their commercial viability. In contrast, YHO is the first inorganic photochromic material with substantial commercial potential for applications in building windows, goggles, helmet visors, and automotive roof glass, achieved without hazardous chemicals during its deposition.

Research on yttrium oxyhydride (YHO) has gained traction among scientists from various countries, including the Netherlands, Sweden, Germany, the USA, China, Latvia, Estonia, and India. Since 2017, YHO and related materials have been key topics at MRS and E-MRS Symposia. In 2018, systematic research led by Smagul Karazhanov culminated in the establishment of Sunphade AS, which began producing YHO-based photochromic films on flexible substrates using roll-to-roll technology in April 2024. Despite over a decade of investigation, the mechanism underlying the photochromic effect remains an open question among researchers.

By the extended X-ray absorption fine structure (EXAFS) for the oxyhydrides of Gd<sup>5</sup> and Y<sup>6</sup>, it was shown that upon air exposure, most O<sup>2</sup>-anions enter the tetrahedral sites of the fcc-lattice. This proves the mixed anion nature of the Gd- and Y-based oxyhydrides. However, no EXAFS study was performed about local structural arrangements around anion vacancies in the transparent and Photodarkened states and no attempt was made to relate it to the photochromism of YHO. Intrinsic point defects and impurities have also been studied by some authors<sup>7-9</sup>. However, the role of the defects in the photochromic properties of YHO is not clarified.

Here by employing first-principles calculations combined with the x-ray diffraction (XRD), extended x-ray absorption fine structure (EXAFS), optical ellipsometry, and ion beam instruments, we report a breakthrough result about the mechanism of the photochromic effect in YHO and of the earlier reported light-induced lattice relaxation.

Yttrium oxide systems, belonging to the category of single-anion materials, represent a promising research frontier due to their considerable potential in advanced technologies. Yttrium primarily exists in the 3+ oxidation state and can adopt three crystal phases: cubic ( $\alpha$ ), monoclinic ( $\beta$ ), and hexagonal ( $\gamma$ ). Trivalent yttrium oxide ( $Y_2O_3$ ) showcases exceptional properties, such as a high melting point (~2700 K), a substantial optical excitation threshold (~5.6 eV), and remarkable mechanical and chemical stability. Growing interest in the 2+ oxidation state has led to investigations into yttrium monoxide (YO). Although early studies began in 2016<sup>4</sup>, there have been no prior reports of divalent yttrium oxide deposition via reactive pulsed-DC magnetron sputtering from a metallic target. This research fills a critical gap in understanding yttrium's oxidation dynamics, marking the first successful production of solid-phase YO through this technique.

# 1.2 Objective of the Thesis

This doctoral research aims to deepen the understanding of yttrium-based double-anion (H, O) system, with particular emphasis on yttrium oxyhydride (YHO) in thin film form and its light-induced chromic properties. Additionally, the study explores yttrium-based single-anion (O) system.

# 1- Yttrium Oxyhydride (YHO) System (Primary Focus):

- I- Role of intrinsic point defects in local structural arrangements in YHO.
- **II-** Role of intrinsic point defects in photochromic properties and lattice contraction in YHO.
- III- Establishing stoichiometry of the YHO films.

# 2- Yttrium Oxide (YO) System (Secondary Focus):

- **I-** Understanding the transition from metallic to fully oxidized states in yttrium thin films, providing insights into the metal-to-oxide transformation process.
- II- Investigating the conditions required to obtain/stabilize divalent yttrium (YO) in the solid phase, contributing to a broader understanding of the chemical and structural factors involved in this less common oxidation state.

# 1.3 Scientific Novelty

#### 1- Yttrium Oxyhydride (YHO) System:

I- By employing EXAFS measurements combined with RMC simulations, we demonstrate that anion vacancies and interstitial hydrogen can cause local structural arrangements that split the radial distribution function (RDF) for Y-Y cations in YHO thin films, a property that persists within the temperature range of 10–300 K.

II- By combining ellipsometry measurements with DFT modeling, we show that anion vacancies form deep-level defect states in the band gap of YHO, which absorb UV/blue light and transfer electrons from the valence band to these defect states. The mechanism of the photochromic effect is related to the absorption of UV/blue light by the defect states, without changing the oxidation state of the majority of Y cations. This finding is consistent with studies of the oxidation state of Y conducted using EXAFS measurements.

**III-** By RBS and ERDA measurements, we demonstrated that the YHO films are not stoichiometric and have a high concentration of anion vacancies.

# 2- Yttrium Oxide (YO) System:

# **Phase Transition Insights:**

**I-** The study reveals how crystalline-amorphous-crystalline (metal-insulator) transitions correlate with variations in oxygen partial pressure during deposition.

II- A previously unreported range of oxygen partial pressures, spanning from ultralow (~10<sup>-7</sup> Pa) to low (~10<sup>-3</sup> Pa), provides new insights into yttriumbased oxide thin film behavior under these conditions.

# Formation and Characterization of Amorphous and Semiconducting Phases:

- I- At an oxygen partial pressure of approximately  $7.57 \times 10^{-5}$  Pa, the material undergoes a transition from crystalline, opaque to a fully amorphous, semi-transparent phase during deposition.
- II- Concurrently, at deposition temperatures near 623 K, semiconducting yttrium monoxide (YO) is formed, coexisting with yttrium oxide (Y<sub>2</sub>O<sub>3</sub>)

in both cubic and amorphous phases, contributing to the semi-transparent nature of the material.

#### 1.4 Author's Contribution

This doctoral research is inherently multidisciplinary, integrating multiple advanced experimental techniques and theoretical calculations to achieve a comprehensive understanding of the materials' properties and behaviors.

The research can be separated into two main sections. The first section covers the production of thin film samples employing magnetron sputtering (DC, Pulsed DC, and High-power impulse) and thermal evaporation (ebeam). Y (by magnetron sputtering and e-beam evaporator), YO (by magnetron sputtering and e-beam evaporator), and photochromic YHO (by e-beam evaporation) thin films were produced in the multi-functional vacuum cluster tool at the ISSP clean room in Riga, Latvia. Y thin film and photochromic YHO, including a large area, were produced at the Institute for Energy Technology clean room in Kjeller, Norway by DC magnetron sputtering. All the material productions were done by the author of the treatise.

The second section involves the characterization of the produced materials, which is divided into two subsections: laboratory-scale characterizations and large-scale research infrastructure based. The laboratory-scale characterizations include Ultraviolet-Visible Spectroscopy (UV-VIS), Spectroscopic Ellipsometry (SE), X-ray Diffraction (XRD), X-ray Photoelectron Spectroscopy (XPS), Scanning Electron Microscopy (SEM), Transmission Electron Microscopy (TEM), Secondary-ion Spectrometry (SIMS), and **Temperature** Dependent Conductivity Measurements (TDCm). The large-scale research infrastructure based characterizations comprise X-ray Absorption Spectroscopy (XAS) at DESY PERTA-III P65 undulator beamline in Hamburg, Germany, as well as Rutherford Backscattering Spectrometry (RBS) and Time-of-Flight Elastic Recoil Detection Analysis (TOF-E ERDA) at the Tandem Laboratory in Uppsala, Sweden.

The Author of the thesis made the following contributions:

Conceptualization and Methodology: The author played a central role in the initial conceptualization of the research, particularly in designing the experimental framework for the laboratory-scale characterizations (UV-VIS, SE, XPS, XRD SEM, TEM, SIMS, TDCm) and the large-scale research

infrastructure based characterizations (XAS, RBS, TOF-E ERDA). This involved defining the objectives, selecting appropriate characterization techniques, and establishing the methodology required to meet the research goals.

Data Collection: The author actively performed/participated in the data collection process, particularly for UV-VIS, SE, TDCm, XAS, XRD, RBS, and TOF-E ERDA. This involved operating sophisticated instrumentation, calibrating equipment, and ensuring the accuracy and reliability of the data obtained from these techniques.

Data Analysis and Interpretation: The author conducted in-depth analyses of the data from UV-VIS, SE, XRD, XPS, SEM, TEM, TDCm, and XAS. The author also interpreted the results in the context of existing literature, contributing to the development of novel conclusions about the properties of the synthesized materials.

Visualization: The author was responsible for the visualization of the data, including the creation of graphs, charts, and other illustrative materials that effectively communicated the findings of the study. This included the visualization of results from UV-VIS, SE, XRD, XPS, SEM, TEM, TDCm, and XAS, ensuring that the data were presented in a clear and accessible manner to support the study's conclusions.

#### Supportive Roles and Computational Section:

The author of this thesis contributed to the analysis and visualization of the results.

# Smagul Karazhanov and K. Vinoth Kumar:

Conducted first-principles calculations pertinent to the research.

#### Alexei Kuzmin:

Directed the X-ray Absorption Spectroscopy (XAS) efforts, including the design of experiments, data acquisition, and analytical processing, and performed EXAFS-related computational work (RMC, DFT).

#### Ilze Aulika:

Directed the Spectroscopic Ellipsometry (SE) studies, focusing on the development of measurement protocols and the analysis of results by Copmelete ESASE (J.A. Woollam).

# 2 METHODOLOGY

The methodology of this research is designed to systematically investigate/represent the production and characterization methods of Y, YO, and YHO thin films. This summary provides an overview of the material production and characterization methods. Detailed experimental procedures for material production and characterization are available in the referenced articles that contribute to this dissertation. The theoretical principles underlying each thin film production method are thoroughly discussed in the main body of the thesis.

#### **Material Synthesis:**

The synthesis phase focuses on the production of thin films using advanced deposition/evaporation techniques. Y, YO, and YHO thin films were produced using both magnetron sputtering (DC, pulsed DC, and high-power impulse) and thermal evaporation (e-beam evaporation). These techniques were chosen for their ability to produce high-quality thin films with precise control over thickness, composition, and uniformity.

Magnetron Sputtering: This technique was employed to deposit Y, YO, and YHO thin films (including large-area YHO) in a controlled vacuum environment at both room and high temperatures. The deposition parameters, such as power, pressure, and substrate temperature, were carefully optimized to produce films with the desired structural properties. Powder samples (YHO) were then obtained by scraping the thin film off the large-area samples produced via this method.

E-beam Evaporation: This technique was primarily employed for the growth of metallic yttrium, fully oxidized yttrium, and photochromic YHO films at room temperature. Evaporation parameters, including e-beam current and chamber pressure (for reactive process), were carefully optimized to achieve films with the desired structural characteristics.

#### **Material Characterization:**

After production, the thin film (and powder) samples were subjected to a comprehensive set of characterizations to assess their structural, chemical, optical, and electronic properties. This characterization phase is divided into two as laboratory-scale and large-scale research infrastructure based techniques.

#### **Laboratory-Scale Characterization:**

Ultraviolet-Visible Spectroscopy (UV-VIS): Employed to measure the optical transmittance and absorbance of YO,  $Y_2O_{3,}$  and photochromic YHO thin films

Spectroscopic Ellipsometry (SE): Used to determine the film refractive index, extinction coefficient, and thickness

X-ray Diffraction (XRD): Applied to assess the crystalline structure and phase composition of the films.

X-ray Photoelectron Spectroscopy (XPS): Utilized to analyze the elemental composition and oxidation states of the elements on the film surface and for depth profiling.

Scanning Electron Microscopy (SEM) and Transmission Electron Microscopy (TEM) are employed to visualize the film morphology and microstructure.

Secondary-Ion Mass Spectrometry (SIMS): Used for depth profiling to determine the distribution of elements (H, O) within the YO film.

Temperature-Dependent Conductivity Measurements (TDCm): Conducted to study the electrical properties of the Y/YO films as a function of temperature.

# **Large-Scale Research Infrastructure Based Characterizations:**

X-ray Absorption Spectroscopy (XAS): Performed at DESY PERTA-III P65 undulator beamline in Hamburg, Germany, to explore the local atomic structure, electronic structure and oxidation states of the elements within the films.

Rutherford Backscattering Spectrometry (RBS) and Time-of-Flight Elastic Recoil Detection Analysis (TOF-E ERDA): Conducted at the Tandem Laboratory in Uppsala, Sweden, to obtain precise elemental composition and depth profiles of the YHO films.

# 3 RESULTS AND DISCUSSIONS

The research findings are divided into two sections: single anion (O) and double anion (O, H) yttrium-based systems, with a major focus on the double anion system, yttrium oxyhydride (YHO).

The first section (Chapter 3.1) focuses on single anion (O) systems, primarily examining yttrium monoxide (YO) properties. It analyzes yttrium oxide thin films deposited under varying oxygen partial pressure levels, showing the structural evolution from metallic yttrium to fully oxidized states. It also details conditions for forming divalent YO at high temperatures.

The second section explores double anion systems, highlighting the role of temperature and light in creating YHO's unique photochromic properties. This part includes atomic-level analyses, temperature effects on structure, and transitions between transparent/bleached and Photodarkened states across Chapters 3.2, 3.3, and 3.4.

#### 3.1 Yttrium/Yttrium Oxide Thin Films

Metallic yttrium/yttrium oxide thin films were deposited at room temperature across ultra-low to moderate oxygen partial pressures to study the transition from metallic yttrium to fully oxidized  $Y_2O_3$  (see Table 3.1 for oxygen levels). X-ray diffraction (XRD) data (Figure 3.1) supports this preliminary analysis. Once the optimal oxygen level for forming an amorphous, semi-transparent phase was identified, high-temperature deposition was conducted to investigate conditions favoring divalent yttrium formation. For details on sputtering and characterization methods, refer to published article  $^{10}$ .

# 3.1.1 Structural Characterization

At room temperature, the films show structural changes depending on oxygen partial pressure (see Figure 3.1a). Oxygen partial pressure is categorized into two regions for electrical properties and three for structural properties. Between ~2 x  $10^{-6}$  and ~4 x  $10^{-5}$  Pa, films exhibit metallic conductivity, with resistivity increasing with oxygen levels in samples  $S_2$ ,  $S_3$ , and  $S_4$ . At ~7.60 x  $10^{-5}$  Pa and above, films become insulating, typical of  $Y_2O_3$  (see Figure 3.3). The structural transformation (Figure 3.1a) involves  $\alpha$ -Y,  $\beta$ -Y<sub>2</sub>O<sub>3</sub>, and  $\alpha$ -Y<sub>2</sub>O<sub>3</sub>, varying with oxygen partial pressure. Sample  $S_7$  at

~7.60 x 10<sup>-5</sup> Pa is X-ray amorphous, marking Region Two, the partial oxidation region for further study.

**Table 3-1** Deposition/evaporation parameters of the Samples. Samples labeled as  $S_{xx}$  were produced using magnetron sputtering, while the sample labeled  $EB_6$  was produced via e-beam evaporation.

Sample	P <sub>O2</sub> Deposition / Evaporation (Pa)	Growth Temperature (K)	Power (W/cm²)
S <sub>11</sub>	~ 2.31 x 10 <sup>-3</sup>	298 ∓5	
S <sub>10</sub>	~ 3.97 x 10 <sup>-4</sup>	298 ∓5	
S <sub>9</sub>	~ 2.11 x 10 <sup>-4</sup>	298 ∓5	
$S_8$	~ 1.26 x 10 <sup>-4</sup>	623 ∓5	
$S_7$	~ 7.60 x 10 <sup>-5</sup>	298 ∓5	~7.4
S <sub>6</sub>	~ 7.55 x 10 <sup>-5</sup>	623 ∓5	
S <sub>4</sub>	~ 4.06 x 10 <sup>-5</sup>	298 ∓5	
$S_3$	~ 1.37 x 10 <sup>-5</sup>	298 ∓5	
$S_2$	~ 2.13 x 10 <sup>-6</sup>	298 ∓5	
			Current on e-Gun
			(mA)
EB <sub>6</sub>	~ 10 <sup>-7</sup>	298 ∓5	~43

In Region 3 (~7.60 x  $10^{-5}$  Pa and above), between ~2 x  $10^{-4}$  and ~4 x  $10^{-4}$  Pa, the film likely consists of  $\beta$ -Y<sub>2</sub>O<sub>3</sub> and  $\alpha$ -Y<sub>2</sub>O<sub>3</sub>. At ~2 x  $10^{-3}$  Pa, it predominantly forms  $\alpha$ -Y<sub>2</sub>O<sub>3</sub>, with a 29° peak suggesting simultaneous  $\alpha$  and  $\beta$ -Y<sub>2</sub>O<sub>3</sub> phases. In Region 1, films (S<sub>2</sub>, S<sub>3</sub>, and S<sub>4</sub>) show metallic conductivity, indicating a metallic yttrium phase. The diffractogram (Figure 3.1a) shows a peak near 31° for  $\alpha$ -Y, shifting to lower angles as oxygen partial pressure increases due to oxygen incorporation and/or sub-oxide formation. A 33° peak in samples S<sub>2</sub> and S<sub>4</sub> is linked to  $\beta$ -Y<sub>2</sub>O<sub>3</sub>.

If oxygen incorporation into the  $\alpha$ -Y structure is the only explanation, discrepancies in the diffractograms for samples  $S_2$ ,  $S_3$ ,  $S_4$ , and  $S_7$  remain unexplained. This prompted further study with an additional metallic yttrium film (Ytf), with deposition details in a forthcoming article. The diffractogram (Figure 3.1b) suggests yttrium crystals and  $\beta$ -Y<sub>2</sub>O<sub>3</sub> form at very low oxygen partial pressures. Another metallic sample (Figure 4.1, eb<sub>3</sub>) also indicates  $\beta$ -Y<sub>2</sub>O<sub>3</sub> as the sub-oxide phase. Nevertheless, thermodynamic calculations<sup>11</sup> propose that the sub-oxide phase is  $\alpha$ -Y<sub>2</sub>O<sub>3</sub> at high temperature.

The variation in peak position observed in samples  $S_2$ ,  $S_3$ , and  $S_4$  is inferred to originate from the formation of the sub-oxide  $\beta$ - $Y_2O_3$  (if the peak around 33° observed in samples  $S_2$ ,  $S_4$ ,  $S_9$ , and  $S_{10}$  is considered

simultaneously). However, the incorporation of oxygen into the host crystal lattice  $(\alpha-Y)$  is also a plausible explanation. The relative contributions of these potential phases are still unclear.

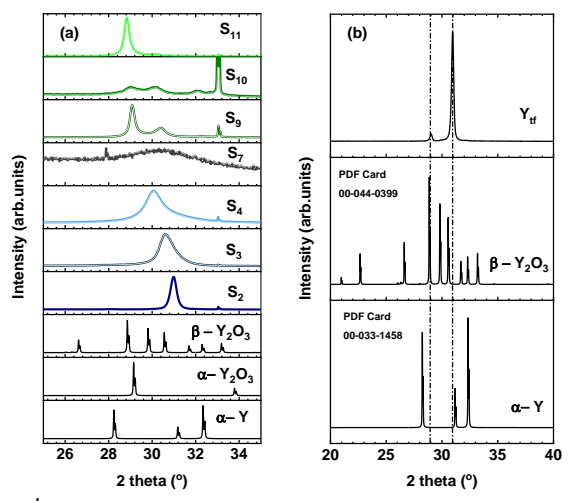


**Figure 3-1** a-X-ray diffraction of samples that were deposited at room temperature along with the reference diffractograms from the ICDD database corresponding from  $\alpha$ -Y (00-033-1458),  $\alpha$ -Y<sub>2</sub>O<sub>3</sub> (01-089-5592),  $\beta$ -Y<sub>2</sub>O<sub>3</sub> (00-044-0399). b-X-ray diffractogram of sample Y<sub>tf</sub> with the same reference diffractograms used in a ( $\alpha$ -Y<sub>2</sub>O<sub>3</sub>, and  $\beta$ -Y<sub>2</sub>O<sub>3</sub>).

A previous study<sup>12</sup> provides a thermodynamic model of the temperature-dependent phase diagram for Y-O systems but lacks specific details for the relevant region.

Current literature lacks comparative experimental and theoretical studies on yttrium in ultralow oxygen environments, sub-oxide formation kinetics, and oxygen-driven structural changes from crystalline metallic yttrium to an insulating amorphous phase. This gap limits definitive conclusions on these processes.

At room temperature, the Region 2 film is X-ray amorphous. To assess temperature effects, a high-temperature ( $\sim$ 623 K) deposition was performed with Sample S<sub>6</sub>. Additionally, a fully oxidized film (S<sub>8</sub>) and a metallic film (EB<sub>6</sub>) using electron beam evaporation (for better vacuum, see Table 3.1) were produced. Comparing these fully oxidized (S<sub>8</sub>), partially oxidized (S<sub>6</sub>), and metallic (EB<sub>6</sub>) films helps clarify the characteristics of the partially oxidized structure.

X-ray diffractograms for samples  $S_6$ ,  $S_8$ , and  $EB_6$  are shown in Figure 3.2a.  $S_8$  (fully oxidized yttrium) and  $EB_6$  (metallic yttrium) show a distinct preferential growth direction.  $EB_6$  also has a peak around  $28^\circ$ , with low intensity, just above the noise level. A peak at  $32^\circ$  may indicate a different phase, though this remains inconclusive. The  $S_6$  diffractogram reveals both amorphous and crystalline phases, requiring further investigation.

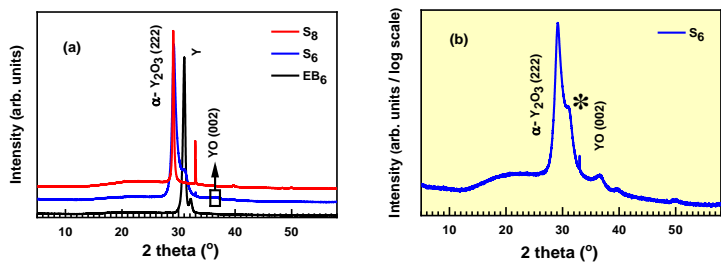


**Figure 3-2** X-ray Diffraction Patterns: X-ray diffraction for samples  $S_6$ ,  $S_8$ , and EB6 shown in (a), with  $S_6$  plotted on a logarithmic scale in (b).

The diffractogram for Sample  $S_6$  (blue line) in Figure 3.2a, separated from fully oxidized and metallic yttrium films, is shown on a logarithmic scale in Figure 3.2b. The crystalline component is mainly  $Y_2O_3$ , with a detectable contribution from YO. The shoulder marked with an asterisk (\*) may indicate YO and/or  $Y_2O_3$ . These results align with existing literature, highlighting the importance of identifying and characterizing the YO phase in a mixed-phase system, as no single-phase YO thin film has been reported.

In our published article  $^{10},$  additional SEM, and TEM measurements were conducted, revealing the related phases (both amorphous and crystalline) and the lattice spacing that could be attributed to YO and/or  $Y_2O_3.$ 

# 3.1.2 Electrical Characterization

If sample  $S_6$  contains YO, it should exhibit characteristic behaviors for thin films, as described in the literature. To confirm this, temperature-dependent electrical conductivity measurements were performed on both YO-containing samples and metallic thin films ( $S_2$ ,  $S_3$ ,  $S_4$ ,  $EB_6$ ), as shown in Figure 3.3.

Sample  $S_6$  exhibits semiconducting characteristics, aligning with literature<sup>4</sup> that indicates YO displays semiconducting behavior. The

semiconducting properties of rare-earth monoxides are not restricted to yttrium; similar behavior has also been observed in YbO<sup>13</sup>, LuO<sup>14</sup>, GdO<sup>15</sup>, EuO<sup>16</sup>, and TbO<sup>17</sup>.

Samples EB<sub>6</sub>,  $S_2$ ,  $S_3$ , and  $S_4$  that represent metallic type electrical conductivity. The deposition/evaporation oxygen partial pressure levels of the sample are given in Table 3.1.

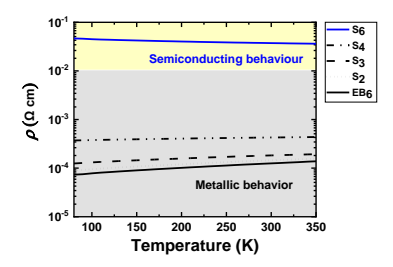


**Figure 3-3** Temperature-dependent electrical resistivity: Samples  $S_2$ ,  $S_3$ , and  $S_4$  (magnetron-sputtered) and  $EB_6$  (e-beam evaporated) exhibit metallic conductivity, while  $S_6$  (magnetron-sputtered) shows semiconducting behavior.

#### 3.1.3 Chemical Characterization

The formation of YO requires the cation to be in a 2+ oxidation state, which warrants further investigation. To explore this, sample  $S_6$  was analyzed using X-ray absorption spectroscopy (XAS), with powder  $Y_2O_3$  and Y metal foil used as reference materials to understand and confirm the 2+ oxidation state.

The results are depicted in Figure 3.4. While there is a clear distinction in absorption edges between  $Y_2O_3$  and Y metal foil, the difference between  $Y_2O_3$  and sample  $S_6$  (which exhibits the simultaneous formation of YO and  $Y_2O_3$ ) is less apparent, (refer to Figure 3.4a). This complexity may arise from factors such as overlapping features and a broad absorption edge, which can affect the relative concentration ratio of YO and  $Y_2O_3$ . It is recommended to refer to article  $^{10}$  where we demonstrated SEM and TEM images of the sample, revealing the material's topological complexity and internal characteristics.

To address this ambiguity, the spectrum is magnified around the absorption edge (refer to Figure 3.4b). Although the separation between the spectra is not significant, the results are consistent with those reported in the prior, singular study available in the literature <sup>4</sup>.

Additionally, plotting the derivative of the X-ray absorption near edge structure (XANES) spectrum is a useful method for distinguishing features

associated with different oxidation states, as shown in Figure 3.4c. This figure displays the distinct shapes of the spectra and corresponding edge energies for different samples (Y foil, cubic  $Y_2O_3$ , and  $S_6$ ), making it easier to differentiate between them.

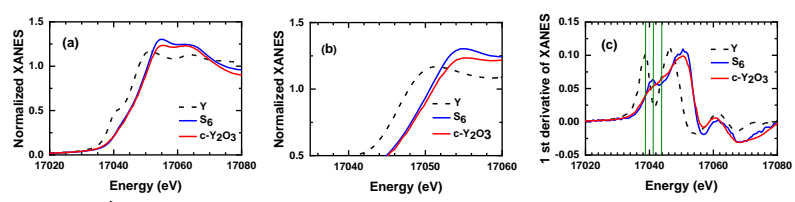


**Figure 3-4** Comparison of XANES spectra: The XANES spectrum of sample  $S_6$  (blue) is compared with Y metal foil (black dash-dot) and  $Y_2O_3$  powder (red). Normalized spectra are in panels (a) and (b), and their first derivatives are shown in panel (c).

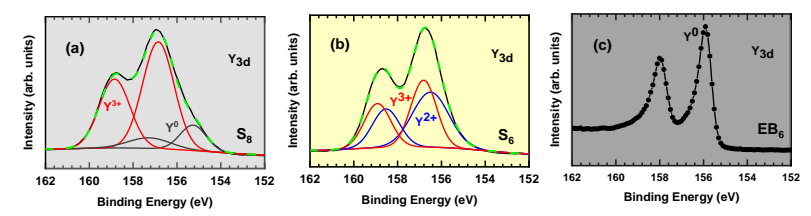
Chemical characterization of samples EB<sub>6</sub>, S<sub>6</sub>, and S<sub>8</sub> was conducted using X-ray photoelectron spectroscopy (XPS), with spectra shown in Figure 3.5. Experimental details are provided in our published article <sup>10</sup>.

Figure 3.5a shows the Y3d spectrum for  $S_8$ , where the peak at 156.85 eV corresponds to  $Y^{3+}$  (Y3ds/2), matching Nefedov et al<sup>18</sup>.'s results. A peak at 155.26 eV likely indicates  $Y^0$  (Y3ds/2)<sup>19,20</sup>, possibly due to Ar<sup>+</sup> interaction. Greczynski and Hultman<sup>21</sup> observed similar binding energy variations in their study, which we also found for  $S_8$ .

Figure 3.5c presents the Y3d spectrum for EB<sub>6</sub>, where a peak at 155.90 eV confirms  $Y^0$  (Y3d<sub>5</sub>/<sub>2</sub>), consistent with Mongstad et al<sup>22</sup>.'s findings.

Figure 3.5b shows the Y3d spectrum for  $S_6$ , where the peak at 156.49 eV indicates  $Y^{2+}$  (Y3ds/2), consistent with literature values for YO<sup>4</sup> and YH<sub>2</sub><sup>23</sup>. A peak at 156.81 eV indicates  $Y^{3+}$  (Y3ds/2), matching reported values<sup>18,24</sup>. These findings confirm the presence of different oxidation states.

Additionally, SIMS measurements were carried out to evaluate the hydrogen content in samples  $S_6$  and  $S_8$ , as illustrated in Figure 3.6. The analysis revealed that the concentration of oxygen in both samples was approximately  $10^2$  times higher than that of hydrogen. This significant disparity in concentration indicates that the amount of hydrogen present is relatively small. Consequently, we can infer that any contribution or contamination from hydrogen in these samples is minimal and unlikely to have a substantial impact on the overall results or properties of the materials.



**Figure 3-5**  $\mid$  X-ray Photoelectron Spectroscopy (XPS) measurements: (a) insulating (S<sub>8</sub>), (b) semiconducting (S<sub>6</sub>), and (c) metallic (EB<sub>6</sub>) behavior. Green dashed lines in (a) and (b) show spectral fitting results.

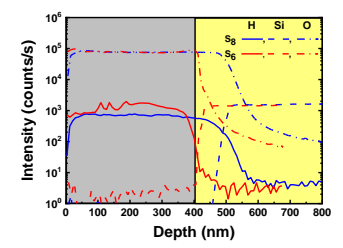


Figure 3-6 | Elemental composition and depth Profiling: Secondary Ion Mass Spectrometry (SIMS) measurements of samples  $S_6$  and  $S_8$ .

# 3.1.4 Optical Characterization

The spectral distribution of optical characteristics ( $\Psi$  and  $\Delta$ ) is essential for distinguishing metals (EB<sub>6</sub>), semiconductors (S<sub>6</sub>), and insulators (S<sub>8</sub>), as shown in Figure 3.7.

The lack of oscillations in the  $\Psi$  and  $\Delta$  spectra for the pure Y (EB<sub>6</sub>) and crystalline mixture (S<sub>6</sub>) samples suggests a high extinction coefficient (k), indicating strong light absorption/reflection and low transparency (see Figure 3.8).

The  $S_8$  sample shows prominent oscillations in the  $\Psi$  and  $\Delta$  spectra (Figure 3.7), typical of a material that is largely transparent. These oscillations result from interference effects within the film, indicating a low extinction coefficient (k) and minimal absorption/reflection (Figure 3.8b).

However, the decreasing amplitude of oscillations above 3 eV (Figure 3.7a) suggests the material starts absorbing light at higher energies, a common behavior for materials that are transparent at lower photon energies but absorb at higher energies near electronic transitions or bandgap.

The refractive index (n) and extinction coefficient (k) as functions of photon energy are derived from  $\Psi$  and  $\Delta$ , as shown in Figure 3.8, using Drude (DO), Gaussian (GO), Tauc-Lorentz oscillator (TLO), and Herzinger-Johs parameterized semiconductor (HJPS) models. For details, refer to our published article<sup>10</sup>.

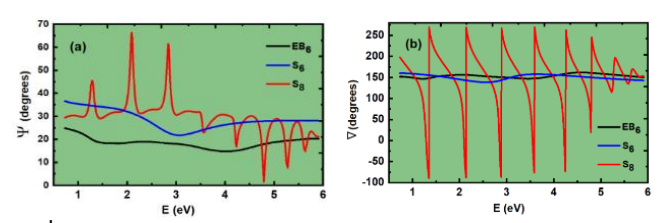


**Figure 3-7** Optical characterization: Main ellipsometric angles  $\Psi$  (a) and  $\Delta$  (b) as a function of photon energy E for samples  $S_6$ ,  $S_8$ , and  $EB_6$ .

The n and k curves for EB<sub>6</sub> show typical metallic behavior: both n and k increase as photon energy decreases from 3 eV to 0.7 eV (black curves in Figure 3.8), with k remaining above 1 for photon energies greater than 3 eV

Sample  $S_8$  ( $Y_2O_3$ ) shows dielectric behavior (Figure 3.8), with n increasing significantly with photon energy, while k rises more gradually, reflecting its relationship to absorption processes. In most dielectrics, significant absorption begins above the bandgap.

The mixed YO and  $Y_2O_3$  material in  $S_6$  (blue curves in Figure 3.8) shows lower k values across the spectrum compared to pure Y, as YO has lower absorption in the visible and near-infrared range and  $Y_2O_3$  has minimal absorption. This results in less overall absorption in the mixed material.

Further characterization focused on the optical excitation threshold of  $S_6$  and  $S_8$ . The optical band gap (Eg) of  $S_8$ , derived from the (HJPS) model, matches literature values  $^{25-27}$ . The absorption in the  $Y_2O_3$  structure within the 2-4 eV range (Figure 3.8b) is attributed to variations in the refractive index (n) and extinction coefficient (k), likely due to film inhomogeneities such as porosity, defects, and compositional fluctuations.

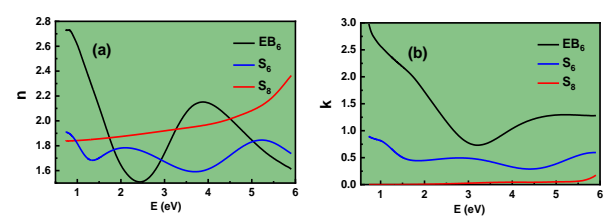


**Figure 3-8** Optical characterizations: Refractive index n and extinction coefficient k as a function of photon energy samples  $S_6$ ,  $S_8$ , and  $EB_6$ .

For sample  $S_6$ , the optical band gap from the Tauc-Lorentz oscillator (TLO) model is  $(0.30\pm0.21)$  eV, in agreement with Kaminaga et al.<sup>4</sup>. Furthermore, the absorbance spectra shown in Figure 3.9 offer additional confirmation of this finding alongside the transmission measurement.

In the broader context of narrow band-gap semiconductors, several related materials have been documented in the literature. TbO<sup>17</sup>, YbO<sup>13</sup>, and LuO<sup>14</sup> are all known for their narrow band gaps.

Since  $S_6$  contains both YO and  $Y_2O_3$ , the high YO volume fraction observed by spectroscopic ellipsometry (details in our published article)  $^{10}$ , suggests a significant amorphous YO phase. This is consistent with literature reports of coexisting monoxide and oxide phases in similar materials  $^{13,14}$  A summary of the refractive index (n), extinction coefficient (k), film thickness (d), surface roughness (Sr), and optical band gap (Eg) for  $S_6$ ,  $S_8$ , and EB<sub>6</sub> is provided in our article  $^{10}$ , along with optical properties of Y, YO, and  $Y_2O_3$  from the literature.

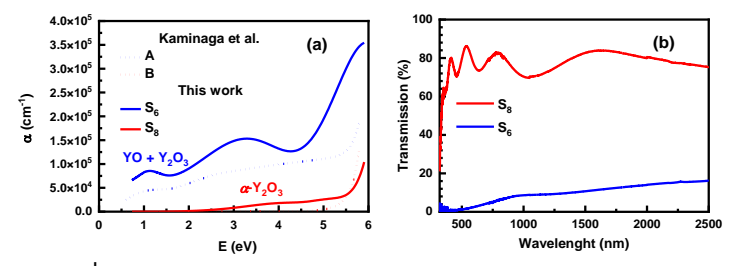


Figure 3-9 | Absorbance and Transmission Comparison: Absorbance of semi-conducting sample  $S_6$  and insulating sample  $S_8$ . (a) Results are compared with literature data: A represents a crystalline  $\alpha$ -Y<sub>2</sub>O<sub>3</sub> and YO mixture, B corresponds to  $\alpha$ -Y<sub>2</sub>O<sub>3</sub>. (b) Transmission measurements of  $S_8$  and  $S_6$ .

# Mechanisms of the Photochromic Effect in Yttrium Oxyhydride Thin Films

Chapters 3.2, 3.3, and 3.4 collectively explore the mechanisms behind the photochromism in YHO thin films. Each chapter addresses a distinct aspect, forming a comprehensive thesis that examines the atomic and nanoscale structures and photochemical processes driving YHO's photochromic behavior.

# 3.2 Photochromic Yttrium Oxyhydride Thin Films

The thin film samples were produced using a focused e-beam evaporator in a vacuum cluster tool within a clean room (ISO 8). The evaporation chamber was baked for 72 hours at 368 K ( $\pm$  5 K) to ensure optimal conditions, with substrate loading and unloading automated via a robotic arm and load lock to maintain vacuum integrity. Substrates were cleaned sequentially in an ultrasonic bath with acetone, isopropanol, and deionized water (15 minutes each) and dried with nitrogen gas. Positioned 26 cm from the crucible, the substrates were placed under a base pressure of 3.00 x  $10^{-5}$  Pa. Thin films of metallic yttrium (eb<sub>3</sub>), oxidized yttrium hydride (eb<sub>4</sub>), and yttrium oxide (eb<sub>5</sub>), each ~200 nm thick, were evaporated at 298 K ( $\pm$  5 K), with reactive gases used for the hydride and oxide films. Detailed procedures are in our published article<sup>28</sup>.

# 3.2.1 Structural and Morphological Characterization

The X-ray diffraction patterns of the samples, shown in Figure 3.10, are compared to the standard JCPDS database. A previous study  $^{29}$  on high-contrast yttrium-based photochromic oxyhydride powder, obtained by scraping a film deposited on a glass substrate, serves as a reference for this discussion and for the samples (film and powder) analyzed in Chapters 3.3 and 3.4. Sample  $eb_3$  is mostly monoclinic, with main peaks around  $2\theta = 31^\circ$ , possibly corresponding to the (002) plane of  $\alpha$ -Y and/or the (401) and (40-2) planes of  $\beta$ -yttria, likely due to yttrium oxidation during evaporation. This supports the findings in Chapter 3.1 of Y metals forming alongside  $\beta$ -yttria. Sample  $eb_5$ , fully oxidized, shows an amorphous or nano-crystalline structure (blue line in Figure 3.10). Sample  $eb_4$ , exhibiting photochromic properties, has a peak around  $29^\circ$  (20), suggesting preferred growth orientation and

potential formation of cubic and/or monoclinic phases of yttria or a cubic  $YH_{1.98}$  phase.

We examined the morphology and structure of sample eb<sub>4</sub> using transmission electron microscopy (Figure 3.11), analyzing films on both glass and silicon substrates to identify any substrate-related structural variations at the nanoscale. The results reveal a previously unreported three-layer structure in the film's cross-section. Similar hydrogen and oxygen-rich regions were observed in a prior study<sup>30</sup> of GdHO structures using atomic probe tomography, suggesting similar behavior in photochromic YHO structures.

The three-layer formation is consistent in lamellas from both silicon and soda-lime glass substrates, with the middle layer around 85 nm thick, while the top and bottom layers vary by approximately 20 nm

A previous study<sup>31</sup> reported a surface oxide layer thickness of 8 nm, while this study found the upper layer to be about 30 nm on silicon and 50 nm on glass. Additionally, a bi-layer yttrium oxyhydride thin film was observed by Komatsu Y. et al.<sup>32</sup>. The cause of the multiple layers remains unclear but likely results from the evaporation process or post-oxidation step.

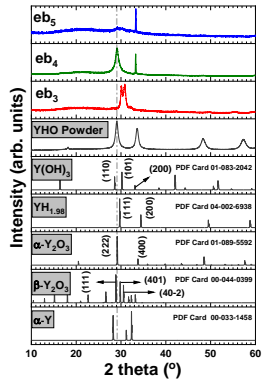


**Figure 3-10** Comparison of XRD Patterns for Yttrium-Based Samples and References: XRD patterns of samples eb<sub>3</sub>, eb<sub>4</sub>, and eb<sub>5</sub> are compared with ICDD references for  $\alpha$ -Y (hcp), Y<sub>2</sub>O<sub>3</sub> (cubic),  $\beta$ -Y<sub>2</sub>O<sub>3</sub> (monoclinic), YH<sub>1.98</sub> (cubic), and Y(OH)<sub>3</sub> (hcp), plus a high-contrast yttrium-based oxyhydride photochromic powder as reference.

TEM measurements were performed on the extracted lamellas with dimensions of only a few hundred nanometers. This extraction process (refer to our published article<sup>28</sup>) could have introduced undesired modifications to the sample. Additionally, the sample was transferred from one vacuum

environment (Focused Ion Beam chamber) to another (TEM chamber), exposing it to an ambient atmosphere during the transfer, which may have caused further modifications. Therefore, the results obtained from TEM could be artifacts and require further clarification.

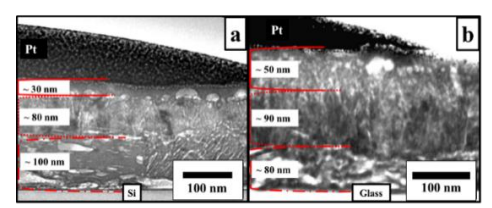


Figure 3-11 | TEM images of extracted lamellas: Layered structure of the sample on a silicon substrate (a) and a soda-lime glass substrate (b), showing consistent layer thickness across both substrates.

#### 3.2.2 Chemical Characterization

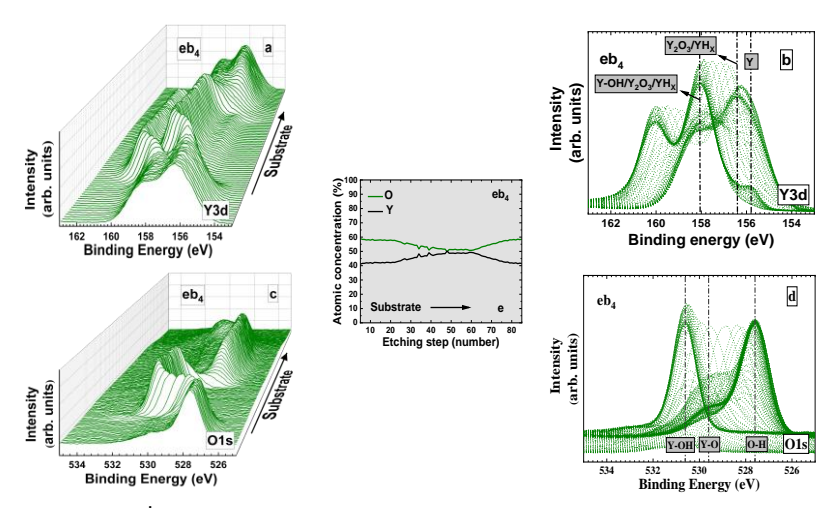
We used X-ray photoelectron spectroscopy, spectroscopic ellipsometry, and ion beam analysis for depth-resolved insights. Figure 3.12 shows XPS data for eb<sub>4</sub>, revealing a three-layer structure in the oxidized yttrium hydride film, which literature typically describes as a two-layer system (see references<sup>31,33</sup>). Depth-resolved XPS analyses for metallic yttrium (eb<sub>3</sub>) and yttrium oxide (eb<sub>5</sub>) are detailed in our published article<sup>28</sup>.

Figure 3.12a shows the Y 3d5/2 spectrum in 3D, categorizing layers into interface and surface. Figure 3.12b provides the 2D spectrum.

The small peak at 155.8 eV suggests  $Y^0$  formation<sup>34</sup>, while the main peak at 156.4 eV indicates  $Y_2O_3$  and/or  $YH_x^{35,36}$ . The peak at 158 eV suggests  $Y_2O_3$ ,  $YH_x$ , or Y-OH, possibly as single or combined phases <sup>23,35,37</sup>.

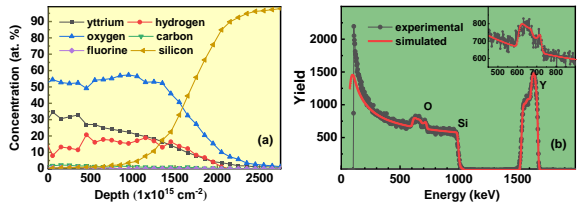
Figure 3.12c shows the depth-resolved O 1s spectrum in 3D, with the 2D view in Figure 3.12d. Peaks around 527, 529, and 530 eV likely indicate O-H, Y-O, and Y-OH formation, respectively<sup>37-39</sup>. The peaks fluctuate due to Ar+ ion interactions, as Ar+ etching's effect on binding energy is well-documented<sup>21</sup> and/or depth resolved nano-scale compositional differences.

Figure 3.12e shows the yttrium-to-oxygen concentration ratio for sample eb<sub>4</sub>, with oxygen concentration decreasing toward the intermediate layer, where it stabilizes at 1:1 (Y). As depth increases, the ratio shifts to 2:3 (Y). This analysis may not capture the full depth profile of the film. A standard binding energy calibration was used, but further studies, including alternative calibrations per Greczynski and Hultman<sup>40</sup> are needed to clarify Y, H, and O bonding (e.g., Y-H, Y-OH, H-Y-O) and their XPS impact.



**Figure 3-12** Depth-resolved XPS analysis of sample eb4: (a) 3D Y 3d spectrum dynamics, (b) Y 3d binding energy density map, (c) 3D O 1s spectrum dynamics, (d) O 1s binding energy density map, (e) Depth-dependent atomic concentration of yttrium and oxygen.

Further depth-resolved compositional analysis of sample  $eb_4$  was conducted to clarify its formation, oxidation, and hydrogenation dynamics. Ion beam techniques (see Figure 3.13) revealed 1-2 at. % C and trace amounts of F, in addition to the primary elements O, H, and Y.



**Figure 3-13** Depth-resolved ion beam analysis of sample eb4: (a) Elemental depth profile from ToF-E ERDA, (b) RBS spectrum with data (black dots) and SIMNRA fit (red line).

The primary element concentrations vary with depth, aligning with TEM and XPS trends. Differences between XPS and ion beam results likely stem from each technique's probing depth and specific measurement locations.

# 3.2.3 Optical Characterization

We used spectroscopic ellipsometry, a nondestructive technique, to examine depth-resolved stoichiometric and chemical variations in the photochromic YHO thin film (sample eb<sub>4</sub>). Similar to our approach with the yttrium single anion system (YO) in Chapter 3.1, we compared YHO with metallic and fully oxidized yttrium here.

Figure 3.14 presents the measured and modeled data ( $\Psi$  and  $\Delta$ ) for samples eb<sub>3</sub>, eb<sub>4</sub>, and eb<sub>5</sub> with mean square error (MSE) values, while Figure 3.15 shows the refractive index (n, k) dispersion curves versus photon energy. Thickness, n, k, surface roughness, and Eg values for all samples are detailed in our published article<sup>28</sup>.

Results for n and k in fully oxidized yttrium films show consistent behavior across both reactive e-beam evaporation and reactive magnetron sputtering methods, confirming optical and structural stability, as expected for  $Y_2O_3$ , yttrium's most stable oxide.

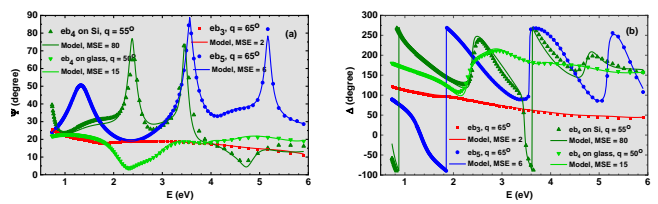


**Figure 3-14** Ellipsometric angles  $\Psi$  and  $\Delta$  vs. photon energy with model fit: (a)  $\Psi$  and (b)  $\Delta$  as a function of photon energy for four samples at a specific incident angle. The continuous line shows the model fit with corresponding MSE values.

Metallic thin films (Chapter 3.1 and 3.2) show similar spectral patterns for n and k values, though these values differ between films made by reactive e-beam evaporation and reactive magnetron sputtering. Both methods exhibit increasing n and k as photon energy decreases, driven by free electron interactions in the metal. These spectral differences likely result from varying oxygen concentrations or sub-oxide phases, as shown in Figures 3.1 and 3.10. We further analysed eb<sub>4</sub> thin films on both substrates, showing a significant optical gradient (see Figure 3.15). The n and k values increase from about 60–100 nm up to 175–220 nm, then decrease toward the surface. The high MSE for eb<sub>4</sub> samples (Figure 3.15) results from inhomogeneities in the YHO films, which the graded EMA model<sup>41</sup> cannot fully capture. In this model, the films are treated as multi-layered, consistent with TEM, XPS, and ion-beam results.

We developed two models to analyse the structure (refer to our published article<sup>28</sup>); here, we discuss the model with the lowest MSE. In this model, the top YHO layer is an EMA mixture with  $Y_2O_3$ , while the middle layer includes a gradient EMA mix of YHO,  $Y_2O_3$ , and Y, assuming YHO as the dominant phase. The increase in (n, k) toward the middle of eb<sub>4</sub> (Figure 3.15) is due to the higher EMA volume fraction of  $Y_2O_3$  and Y, whose n and k values at 1.67 eV exceed those of YHO. The rise in k around 150 nm and 200 nm for eb<sub>4</sub> on glass and Si, respectively, suggests a larger volume fraction of Y.

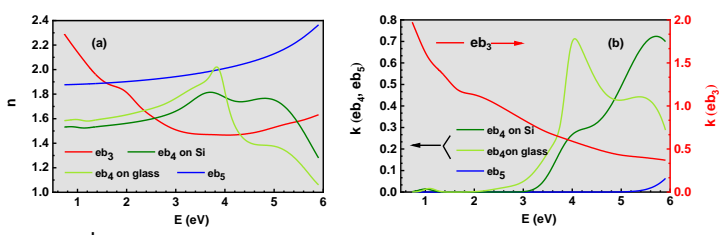


**Figure 3-15** Refractive index (n) and extinction coefficient (k) vs. photon energy: (a) n and (b) k as functions of photon energy for samples  $eb_3$ ,  $eb_4$  on Si and glass substrates, and  $eb_5$ .

XPS data indicate an interphase layer, likely containing Y metal (see Figure 3.12), near the film's bottom layer. Note that the XPS spectrum may not capture the full sample thickness. This observation may be affected by  $Ar^+$  etching effects on binding energy or by measurements from areas with varying inhomogeneities.

The increase in Y and  $Y_2O_3$  content toward the middle of the film from SE is consistent with the XPS data (see Figure 3.12). These depthresolved characterizations reveal that the photochromic YHO thin film exhibits stoichiovariants characteristics, with distinct regions rich in oxygen and/or hydrogen and three identifiable layers. This is the first study to identify these features in the YHO structure.

A previous<sup>30</sup> proposed mechanism for photochromism in rare-earth-based oxyhydride systems (such as GdHO, and YHO) was based on the formation of multiple phases, including RE<sub>2</sub>O<sub>3</sub> and REH<sub>2</sub> (RE: Gd, Y).

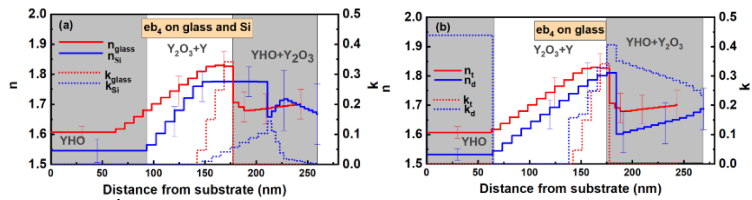


**Figure 3-16** Depth profile of eb<sub>4</sub> at 1.67 eV on (a) both substrates and (b) transparent and dark state (glass substrate).

The photochromic effect of sample  $eb_4$  was tested in reflection and transmission modes before and after UV illumination. Figure 3.17 shows the complex dielectric functions (n and k) and experimental and modeled transmission spectra in both transparent and dark states. The extinction coefficient increases from 3.5 eV to the infrared range in the dark state, indicating significant structural changes, as seen in the depth profile (Figure 3.16b). The YHO thin film's photochromic efficiency is higher than previously reported. Table 3.2 summarizes the gap energies (Egap) for the three peaks in the (n; k) dispersion curves, with the refractive index decreasing, the extinction coefficient increasing, and energy gaps for direct transitions decreasing in the dark state.

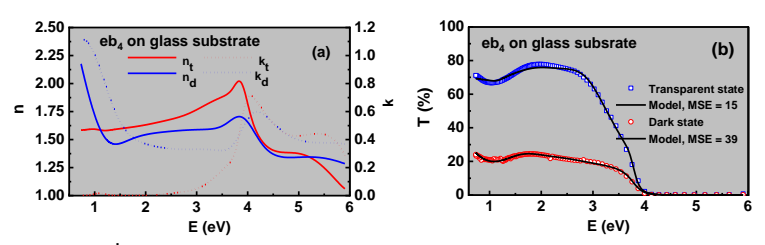


**Figure 3-17** Measured and modeled transmission spectra: (a) and complex refractive index dispersion curves (b) for sample eb<sub>4</sub> on glass in transparent and dark states.

The potential origin of the spectral variation in the refractive index n (see Figure 3.17a) concerning the reported optical excitation thresholds will be explored in detail in Chapter 3.4. This chapter will provide a comprehensive discussion of how these variations are linked to the underlying mechanisms affecting the optical properties.

Table 3-2 Optical Properties of sample on different substrates. The electron transition energies  $E_{gap}$ , n, and k at 550 nm for thin film on Si and glass substrates.

	$E_{gap}$ , eV		n		k	
Substrate	Transparent (T)	Dark (D)	T	D	T	D
Si	$3.50 \pm 0.20$ $2.68 \pm 0.39$ $0.56 \pm 0.21$	-	1.58 ± 0.04	-	0	-
SiO <sub>2</sub>	$3.48 \pm 0.05$ $1.60 \pm 0.40$ $0.41 \pm 0.20$	$3.15 \pm 0.29$ $1.16 \pm 0.33$ $0.11 \pm 0.10$	1.66 ± 0.02	1.56 ± 0.04	0.007 ± 0.001	0.35 ±0.02

#### 3.2.4 Chemical and Structural Characterization

The XAS analysis was divided into two parts. The first focused on the XANES region, up to the absorption edge, to examine the oxidation state of the cation in each sample. Figure 3.18 shows the experimental spectra and first derivatives for the samples and references. The Y K-edge XANES spectra are dominated by the  $1s(Y) \rightarrow np(Y)$  transitions. The first maximum of the XANES derivative occurs at 17038 eV for yttrium foil. The absorption edge for the metallic yttrium thin film (eb<sub>3</sub>) is at 17039 eV, indicating partial oxidation, consistent with XPS, XRD, and SE data. The absorption edge for yttrium oxide (eb<sub>5</sub>) and bulk Y<sub>2</sub>O<sub>3</sub> is at 17041 eV, indicating full oxidation of yttrium (3+). YHO powder and the oxidized yttrium hydride thin film (eb<sub>4</sub>) have an edge at 17040.5 eV, suggesting an oxidation state of approximately 2.5+. The second part of the study analysed the local structure of the cation using EXAFS. The Y K-edge EXAFS spectra  $\gamma(k)k^2$  and Fourier transforms (FTs) are shown in Figure 3.19a-b. The EXAFS spectra and FTs of yttrium foil and the metallic yttrium thin film (eb<sub>3</sub>) are nearly identical, indicating no anionic contributions in the local structure. The EXAFS spectra of yttrium oxide (eb<sub>5</sub>) and bulk Y<sub>2</sub>O<sub>3</sub> show similarities, but the FTs of eb<sub>5</sub> have reduced peak amplitudes, indicating disorder and a nanocrystalline structure 42,43, consistent with XRD results. Note that the FT peak positions differ from crystallographic values due to phase shifts in EXAFS.

The EXAFS spectrum and FT for the oxidized yttrium hydride film (eb<sub>4</sub>) closely resemble those of YHO powder. The peak positions for the first (cation-anion) and second (cation-cation) coordination shells are nearly identical, though the amplitudes, reflecting anion density, show some variation. Literature (e.g., Reference<sup>29</sup>) does not specify the exact number or positions of anions in photochromic YHO structures, a topic to be discussed in Chapter 3.3. Local structural analysis of the photochromic YHO sample

(eb<sub>4</sub>) and  $Y_2O_3$  (eb<sub>5</sub>) was further explored using reverse Monte Carlo simulations, as detailed in our published article<sup>28</sup>.  $Y_2O_3$  has two distinct yttrium sites in its cubic structure (Ia-3)<sup>43</sup>, located at Wyckoff positions 8b (0.25, 0.25, 0.25) and 24d (u, 0, 0.25), with u = -0.0326 at 300 K<sup>44</sup>. Both yttrium atoms are octahedrally coordinated by oxygen. The second coordination shell of yttrium in sample eb<sub>4</sub> (Y-Y) consists of two groups of six yttrium atoms at approximately 3.5 Å and 4.0 Å.

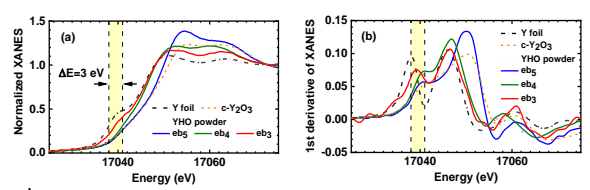


**Figure 3-18** Normalized Y K-edge XANES spectra (a) and first derivatives (b) for thin films eb<sub>3</sub>, eb<sub>4</sub>, and eb<sub>5</sub>, compared with reference compounds (yttrium foil, bulk c-Y<sub>2</sub>O<sub>3</sub>, and YHO powder). Dashed vertical lines indicate absorption edge positions for reference materials.

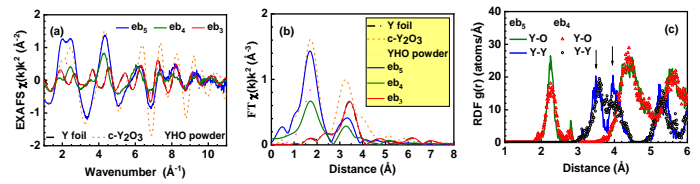


Figure 3-19 Y K-edge EXAFS Analysis of Thin Films: (a) Y K-edge EXAFS spectra  $\chi(k)k^2$  and (b) their Fourier transforms (FTs) for eb<sub>3</sub>, eb<sub>4</sub>, and eb<sub>5</sub> thin films, compared with reference compounds (Y foil, bulk c-Y<sub>2</sub>O<sub>3</sub>, and YHO powder), showing only the FTs' moduli. (c) Partial radial distribution functions (RDFs) g(r) for Y-O and Y-Y in eb<sub>4</sub> (open symbols) and eb<sub>5</sub> (solid lines), derived from Y K-edge EXAFS spectra using the RMC method. Arrows highlight two yttrium atom groups in the second shell.

RMC results for samples  $eb_4$  and  $eb_5$  showed a split in the second coordination shell (Y-Y) for both. The findings for fully oxidized yttrium  $(eb_5)$  are consistent with literature<sup>43</sup>. In the oxidized yttrium hydride film  $(eb_4)$ , increased disorder in the first coordination shell reduces the first peak, broadening the cation-anion distribution. The second shell splitting is less pronounced, with the 4 Å peak becoming broader. These results suggest at least two distinct cationic geometric structures. Temperature and light effects on the structure will be discussed in their respective Chapters 3.3 and 3.4.

# 3.3 Temperature-Dependent Structural Variation in Photochromic Yttrium Oxyhydride

Chapter 3.2 explored the possible causes of splitting in the second cationic coordination shell around Y in photochromic YHO structures. This chapter further investigates the effect of temperature, particularly at cryogenic levels. The YHO powder used was scraped from a large-area substrate. Details on sample production, characterization, and computational research can be found in the referenced article <sup>45</sup>.

# 3.3.1 Optical Characterization

The photochromic properties of the YHO thin film are shown in Figure 3.20. Transmission measurements were calibrated against air transmission, covering the 300 nm to 1000 nm range. Samples were illuminated for 30 minutes with a 405 nm Laser Diode at 4.5 mW cm<sup>-2</sup>. For cyclic testing, the average optical transmission between 650 nm and 850 nm was monitored over 30 minutes with alternating laser on and off states.

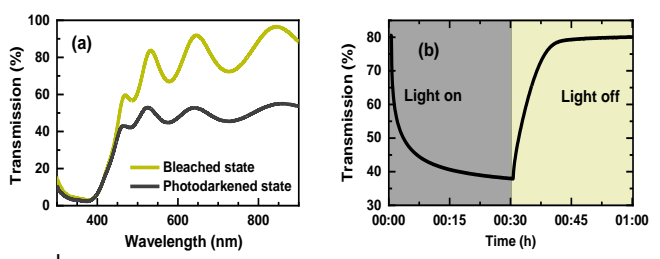


**Figure 3-20** Photochromic efficiency of YHO: (a) Transmission measurements of the YHO sample on glass in transparent and Photodarkened states. (b) One-hour cycling test of the photochromic YHO sample on glass in a laboratory environment.

# 3.3.2 Structural Characterization

The procedure starts with XRD analysis (Figure 3.21a), which, along with refinement, is the sole method used in this thesis, confirming that photochromic YHO primarily forms in the Fm-3m crystal structure.

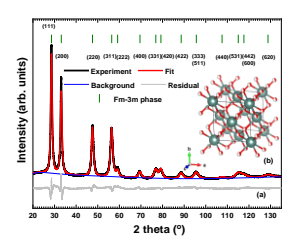


**Figure 3-21** Structural characterization of photochromic YHO: (a) X-ray diffraction of the sample with refinement. (b) Unit cell representation of YHO, with grey spheres for yttrium, and white/red spheres for oxygen and hydrogen at interstitial sites.

Refinement of the Bragg peaks was done using the cubic space group Fm-3m (225). The structural model<sup>29</sup>, based on previous synchrotron and neutron diffraction work, shows yttrium and oxygen atoms occupying Wyckoff positions 4a (0,0,0) and 8c (0.25,0.25,0.25), respectively, with yttrium forming an fcc sub-lattice surrounded by up to eight oxygen atoms in the first coordination shell (Table 3.3).

**Table 3-3** | **Refined structure parameters for the sample from XRD.** The cubic (space group Fm-3m (225)) lattice parameter a = 5.404(3) Å. Crystallite size d = 16(2) nm.

Element	Wyckoff position	Atomic coordinates	Occupation	B <sub>iso</sub> (Å <sup>2</sup> )
Y	4a	0, 0, 0	1	1.5(1)
O	8c	0.25, 0.25, 0.25	0.40(2)	5.2(3)

Unlike the referenced study<sup>29</sup>, which used neutron diffraction to propose Wyckoff positions for hydrogen, our study did not include this due to X-rays' weak sensitivity to hydrogen.

The measured lattice constant, a = 5.404(3) Å, is slightly larger than the reported value of a = 5.3226(3) Å in reference<sup>29</sup>, likely due to the smaller crystallite size (d = 16(2) nm) in our sample.

As noted in reference<sup>29</sup> and confirmed by our research, the interstitial positions and anionic concentration are uncertain. To clarify the cationic structure, we used X-ray absorption spectroscopy. This chapter focuses on the origin of the observed splitting in the second coordination shell around yttrium, with the EXAFS spectrum further discussed in Chapter 3.4.

# 3.3.3 Radial Distribution Function Analysis

The RMC method, using an evolutionary algorithm approach <sup>46,47</sup> was employed. Experimental and calculated temperature-dependent k-weighted EXAFS signals and their Fourier transforms are given in Figure 3.22. Further details of the simulation are available in our published article<sup>45</sup>.

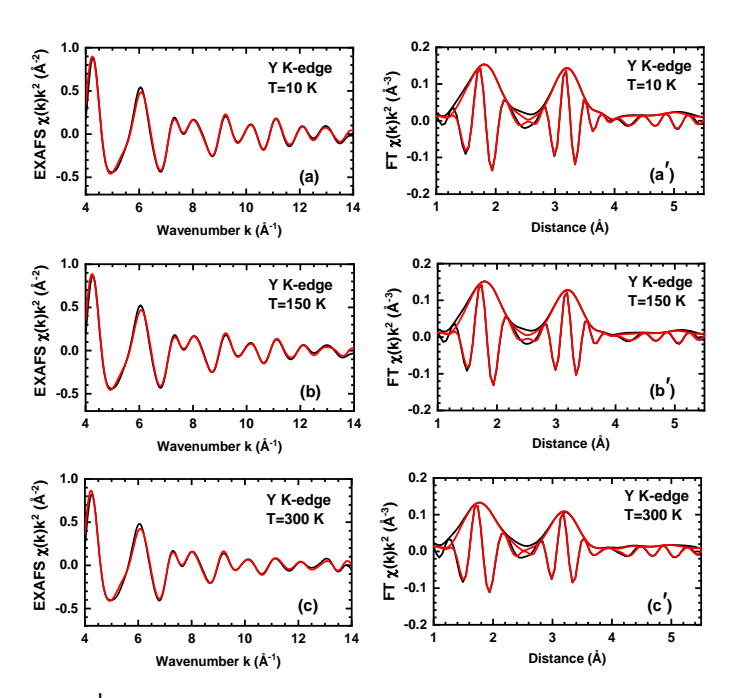
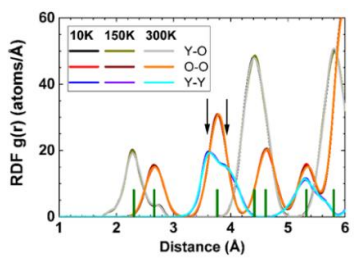


Figure 3-22 | Temperature-dependent EXAFS of powder YHO. Experimental (black) and RMC-calculated (red) Y K-edge EXAFS spectra  $\chi(k)k^2$  (a, b, c) and their corresponding Fourier transforms (a', b', c') at (a; a') 10 K, (b; b') 150 K, and (c; c') 300 K.

The temperature-dependent radial distribution functions (RDFs) for atomic pairs (Y-Y, Y-O, O-O) from the RMC are shown in Figure 3.23. These RDFs, measured at different temperatures, show minimal thermal disorder. At higher temperatures, only the first peak at 2.3 Å, representing the anionic coordination shell, shows a slight broadening.



**Figure 3-23** Temperature-dependent RDFs of Y-O, O-O, and Y-Y in YHO powder: The RDFs at 10, 150, and 300 K were derived using the RMC method from Y K-edge EXAFS spectra. Coordination shell positions are marked with vertical bars from XRD data, and arrows highlight Y-Y splitting in the second coordination shell.

The peak positions in the partial RDFs align well with the crystallographic structure predictions (indicated by vertical bars in Figure 3.22), except for the second coordination shell of yttrium. The peak at 3.8 Å in the Y-Y RDF is broadened and split into two components at 3.6 and 3.9 Å. This splitting is inconsistent with the commonly accepted cubic Fm-3m structure (reference<sup>29</sup>) and our XRD results (Figure 3.21), where all yttrium atoms are equivalent. It also conflicts with any structure where yttrium forms a perfect fcc lattice. This suggests local distortions in the YHO structure, particularly around yttrium, though they are minimal and not detectable by diffraction. These distortions may result from variations in Y-O and Y-H bond interactions, to be explored further in Chapter 3.4.

The splitting in the second coordination shell around Y in YHO is not an artifact but a consistent experimental finding, as shown in this and Chapter 3.2. As YHO is a stoichiovariants material, the cause of this splitting and its dependence on the anionic ratio will be explored through first-principles DFT calculations on three YHO models with different anionic ratios.

In the first model, all yttrium atoms are surrounded by eight oxygen atoms, maintaining high-symmetry Wyckoff positions and no distortion in the second Y-Y shell (Figure 3.24, black curve).

In the second model, replacing ten oxygen atoms with hydrogen introduces asymmetry around yttrium, distorting the second Y-Y shell (Figure 3.24, red curve).

In the third model, replacing eleven oxygen atoms with hydrogen and adding an extra hydrogen atom causes the second Y-Y shell to split into two distinct peaks (Figure 3.24, blue curve).

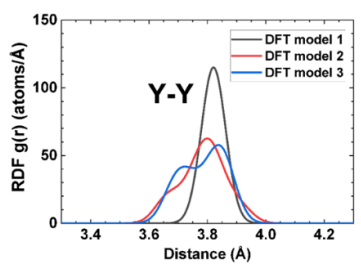


**Figure 3-24** RDFs for Y-Y distance in YHO with anionic ratios: Partial RDFs for Y-Y interatomic distance in the second coordination shell, obtained from DFT calculations for three models with O ratios of 1:0 (model 1), 2:5 (model 2), and 5:12 (model 3).

DFT calculations show that the distortion in the second Y-Y shell results from local symmetry breaking due to hydrogen incorporation, with anionic imbalance playing a key role in the splitting. However, the splitting shows minimal temperature dependence.

# 3.4 Role of Anion Vacancies and Lattice Dynamics in Photochromic Yttrium Oxyhydride

In this chapter, we investigate the light-induced structural changes of magnetron-sputtered photochromic YHO at both nano and atomic scales, which is identical to the material analyzed in previous chapters (3.2 and 3.3). For detailed experimental methods, refer to the relevant article<sup>48</sup>.

## 3.4.1 Optical and Nanoscale Structural Characterization

The investigation began with XRD and transmission measurements of the YHO thin film in its transparent state. The sample was then exposed to UV light under laboratory conditions, and the measurements were repeated for both the Photodarkened and bleached states. The corresponding optical and structural results are presented in Figures 3.25 and 3.26, respectively.

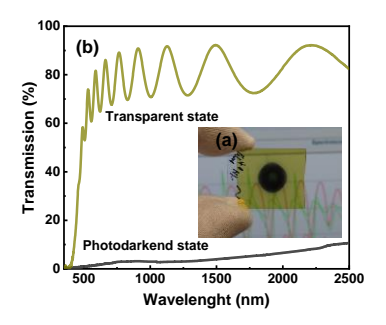


**Figure 3-25** Light-induced optical changes in YHO: (a) Visual of the YHO thin film on glass, with a central Photodarkened spot and a transparent, greenish region. (b) Transmission measurements of the regions in (a), showing the optical properties of the Photodarkened and transparent states.

Figure 3.25 illustrates the significant change in transmission of the YHO thin film on a glass substrate upon illumination. Figure 3.25a shows the Photodarkened center, while the surrounding area remains transparent. This transition occurs over an energy range of 0.5 to 4 eV, as shown in Figure 3.25b. The results confirm the high UV sensitivity of the YHO material. X-ray diffraction (XRD) measurements of the sample in its transparent, Photodarkened, and bleached states are presented in Figure 3.26a. Our findings align with a previous study<sup>49</sup>, which reported light-induced lattice

contraction. Lattice parameters for each state are calculated and shown in Figure 3.26b. The light-induced nanoscale structural changes observed in the XRD data, coupled with the absence of a clear explanation, led us to explore the material at the atomic scale.

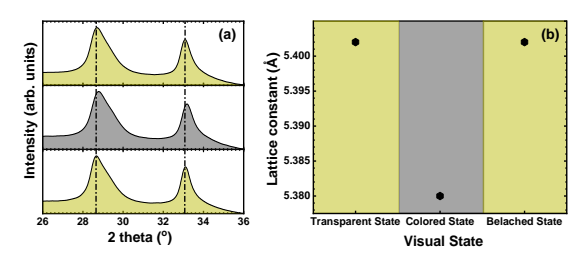


**Figure 3-26** Light-induced structural changes in YHO: (a) XRD patterns of YHO in its transparent, Photodarkened (colored), and bleached states, showing structural variations. (b) Lattice parameters for the corresponding states in (a).

# 3.4.2 Light-Induced Chemical and Structural Characterization

We used X-ray absorption spectroscopy to analyze the local structure around the Y sites, focusing on two regions: 1) XANES and 2) EXAFS. Starting with the XANES region (Figure 3.27), we observed features indicative of the oxidation state, electronic structure, and coordination environment of yttrium. Both films displayed a shoulder (region 1) and two prominent peaks (regions 2 and 3), linked to transitions of Yttrium 1s electrons into Y p-states hybridized with oxygen p-states. XANES measurements for the transparent and Photodarkened states show no shift in the absorption edge (region 1, Figure 3.27), indicating no detectable change in cationic oxidation state due to light exposure, with Y cations remaining at an oxidation state of about 2.5+ (Chapter 3.2).

We are now shifting to the EXAFS region to investigate light-induced structural changes in the cations. The EXAFS spectrum and its Fourier transform (Figure 3.28) show light-induced variations in the first and second coordination shells of yttrium, with increased peak amplitudes at 1.8 and 3.3 Å in the Fourier transforms. The difference in the second coordination shell, particularly at the Y-Y distance, was further analyzed using RMC methods (Figure 3.29), with details available in the related article. Atomic coordinates from RMC calculations were used to compute the partial radial distribution functions (RDFs) for Y-O and Y-Y in both transparent and

Photodarkened YHO films (Figure 3.29). This analysis reveals that the second coordination shell of yttrium splits into two peaks at 3.62 Å and 3.98 Å, a splitting that remains even in the transparent state, indicating variations induced by visible light.

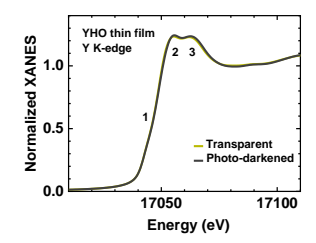


**Figure 3-27** Normalized XANES spectra: Spectra for the transparent and Photodarkened states of YHO thin film.

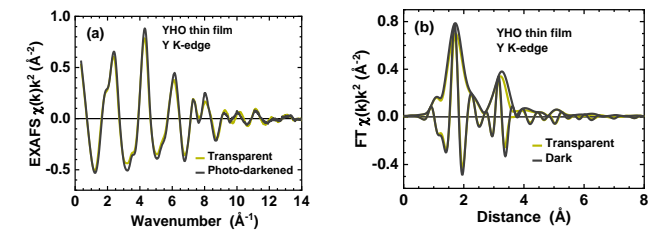


**Figure 3-28** Local Structure Analysis of YHO: EXAFS Fourier Transforms and  $\gamma(k)k^2$ 

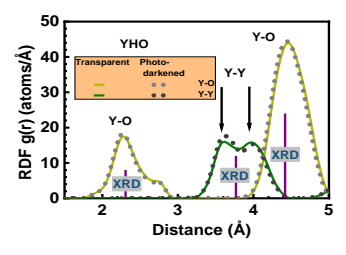


**Figure 3-29** RDFs of YHO Thin Film: Transparent vs. Photodarkened States. Partial RDFs for Y–O and Y–Y in transparent (solid) and photodarkened (dotted) YHO thin films, derived from Y K-edge EXAFS spectra using the RMC method. Coordination shell positions are marked by vertical bars, based on X-ray diffraction data.

# 3.4.3 Relationship Between Atomic-Scale and Nanoscale Structural Variations

We connect atomic-scale and nanoscale structural variations by introducing a new approach that examines anionic vacancies in YHO structures. XAS data show that while most cations remain unchanged, visible light induces a structural change. Figure 3.26a (XRD data) shows that UV light causes reversible lattice relaxation in YHO, with contraction during exposure and expansion afterward. First-principles calculations reveal that UV exposure increases anionic vacancies, while their removal boosts cationic vacancies.

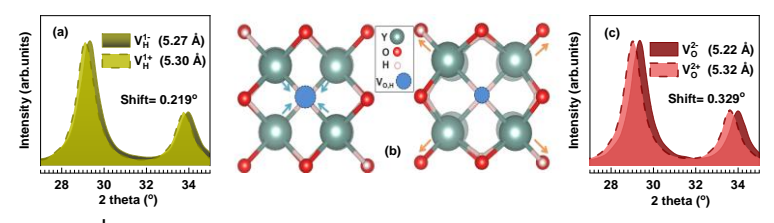


**Figure 3-30** Light-Induced Structural Changes in Yttrium Oxyhydrides: (a) XRD peak shifts and lattice constants for VH; (b) Light-induced local structures around VH<sup>1-</sup>, VO<sup>2-</sup> (left) and VH<sup>1+</sup>, VO<sup>2+</sup> (right) in YHO; (c) XRD peak shifts and lattice constants for VO.

These vacancies explain why the oxidation state of most cations remains unchanged despite structural variations. The presence of anionic vacancies also accounts for YHO's deviation from the ideal Fm-3m structure, as discussed in Chapters 3.2 and 3.3. Additionally, RDF results<sup>43</sup> for Y<sub>2</sub>O<sub>3</sub> show splitting in the second Y-Y coordination shell, indicating two distinct octahedral environments linked to anionic vacancies.

## 3.4.4 Electronic Structure and Optical Characterization

Anion vacancies play a key role in light-induced structural changes. In photochromic YHO, these vacancies create localized energy states within the band gap, enhancing absorption or reflection of sub-bandgap photons. Figure 3.31 shows the modified electronic band structure with  $VO_2^+$  (red lines) and  $VH^+$  (green line), derived from hybrid functional calculations. Ideal YHO's electronic structure, with an optical excitation threshold around 3.9 eV, is detailed in our article<sup>48</sup>. Depending on their charge, VO and VH

introduce distinct energy levels in the band gap.  $VH^+$  creates a band ~2.3 eV above the valence band (Figure 3.31a), while  $VO_2^+$  produces bands near 1.0 eV (infrared) and 3.0 eV (UV) (Figure 3.31b). Changes in charge states affect these levels. Anionic vacancies in YHO alter its electronic band structure, leading to absorption of specific wavelengths and resulting in a darkening of the material. This photochromism, driven by anion vacancies, has also been observed in materials like  $Al_2O_3^{50}$ ,  $BaMgSiO_4^{51}$ , and aluminosilicate group such as hackmanite, tugtupite, and scapolite<sup>52</sup>.

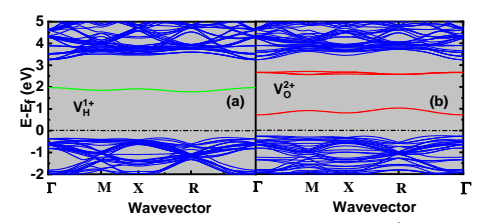


**Figure 3-31** Modified Band Structure of YHO: (a) VH<sup>1+</sup> for hydrogen vacancies and (b) VO<sup>2+</sup> for oxygen vacancies.

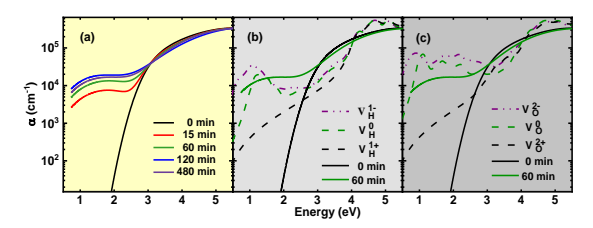


**Figure 3-32** Time-Resolved Absorption and Anion Vacancy in YHO Films: (a) Absorption coefficient spectrum at 0, 15, 60, 120, and 480 minutes of UV exposure. (b) Absorption coefficient for films with hydrogen vacancies and (c) with oxygen vacancies, compared to experimental data at 0 and 60 minutes.

Time-resolved spectroscopic ellipsometry (trSE) was used to investigate the optical properties of YHO thin films, as shown in Figure 3.32a. In the transparent state, the absorption coefficient in the visible range is negligible, attributed to the localized nature of anion vacancy states (Figures 3.32b and 3.32c). The theoretical absorption coefficients for YHO with various hydride and oxide anion vacancies align well with trSE results for Photodarkened films. The strong visible absorption is primarily due to these vacancies, with some discrepancies likely arising from fitting uncertainties and the complex nature of the defect spectra.

### 4 SUMMARY AND CONCLUSION

This treatise aims to provide a comprehensive understanding of yttrium-based systems, primarily focusing on yttrium oxyhydride (YHO) as a double-anion system (H, O), while also addressing yttrium monoxide (YO) as a single-anion system (O).

In the single-anion system, we investigated the growth kinetics of yttrium/yttrium oxide thin films across ultralow to moderate oxygen partial pressures. Our findings reveal that during thin film deposition/evaporation at low/ultralow oxygen partial pressures, yttrium predominantly forms a hexagonally structured metallic phase, accompanied by sub-oxides. Based on our analysis, we propose that  $\beta$ -Y<sub>2</sub>O<sub>3</sub> is the most probable sub-oxide under ultralow oxygen partial pressures. As the oxygen partial pressure increases, oxygen atoms integrate into the metallic crystal lattice and/or facilitate the formation of additional sub-oxide phases. This process gradually leads to the material's amorphization, transitioning it into an electrically insulating state, ultimately resulting in full amorphization. At sufficiently high oxygen levels, fully oxidized Y<sub>2</sub>O<sub>3</sub> crystals form at room temperature. Nevertheless, the precise upper and lower oxygen partial pressure limits for the concurrent formation of metallic yttrium crystals and sub-oxides in yttrium/yttrium oxide thin films remain unclear. In the partial pressure range where the material becomes fully amorphous, deposition at elevated temperatures promotes the formation of semiconducting yttrium monoxide (YO) alongside Y<sub>2</sub>O<sub>3</sub>.

In the double anion system, the structural characteristics of photochromic YHO are explored at both nanoscale and atomic levels, along with the effective oxidation state of the cations. Our analysis examines YHO's photochromic behavior from three different perspectives, offering a deeper understanding of its light-induced kinetics. We propose that photochromic YHO has a stoichiovariants nature, with most yttrium atoms exhibiting an oxidation state around 2.5+, a state that remains stable between bleached and photo darkened conditions. The distorted face-centered cubic (FCC) structure of YHO shows splitting in the second coordination shell around the yttrium, caused by the addition of extra hydrogen atoms and random substitution of oxygen by hydrogen within the FCC lattice. This splitting points to the presence of two broad families of distinct cationic geometric structures, each potentially containing multiple configurations. In the literature, a similar phenomenon is observed in  $Y_2O_3$ , where yttrium atoms are coordinated by oxygen atoms in two distinct octahedral environments.

Moreover, the observed shell splitting in the transparent state shows subtle temperature dependence, further emphasizing the complexity of the system. We also suggest that the light-induced structural variations observed through XRD are closely tied to localized movements of anionic defects, which induce distortions in the second coordination shell around the yttrium.

We have also observed a correlation between single-anion and double-anion systems. Yttrium's propensity to form sub-oxide phases under ultralow oxygen partial pressures during the deposition or evaporation of YH thin films (considered the initial state for producing photochromic YHO) suggests that the film may consist of a mixture of YH, YO, or even YHO. This simultaneous formation appears to be directly linked to the photochromic performance of YHO.

To explore this further, we monitored the evolution of residual gas species during the deposition of yttrium hydride (YH) and yttrium (Y) thin films using a mass spectrometer. The detailed results of these measurements will be presented in a separate study. Figure 4.1 highlights the fluctuations in partial pressures of key residual gases, including hydrogen (H<sub>2</sub>), oxygen (O<sub>2</sub>), and water vapor (H<sub>2</sub>O), over time, providing insights into the deposition process. During YH thin film deposition, hydrogen plays a vital role in promoting oxygen absorption. The resulting hydrogen-oxygen interactions are likely absorbed or accumulated by components within the process chamber, including the deposited film, target surface, and inner chamber elements. For Y thin films, residual gas behavior is similar, although hydrogen exhibits more pronounced variations during deposition and is highly sensitive to changes in partial pressure levels.

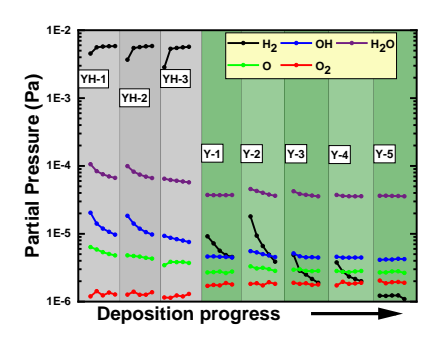


Figure 4-1 | Residual gases kinetics during YH and Y metal thin film deposition. This image represents the time evolution of residual gas species observed during the deposition of yttrium hydride (YH) and yttrium (Y) metal thin films.

Additionally, we conducted a comparative chemical study between photochromic YHO and semiconducting YO, revealing that the effective oxidation state of yttrium in both materials is approximately 2.5+ (refer to Figure 4.2).

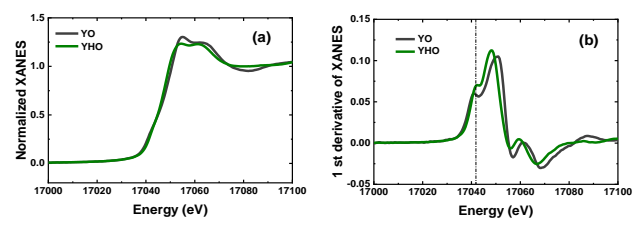


Figure 4-2 XANES studies of photochromic YHO and semiconducting YO thin films. (a) normalized XANES spectra of the materials, with YHO representing the transparent state; (b) the first derivative of the corresponding spectra.

### **Main Theses**

- 1- Yttrium/yttrium oxide thin films, during deposition or evaporation under ultralow oxygen partial pressure (~10-7 Pa), predominantly form as metallic yttrium with a hexagonally oriented structure, accompanied by sub-oxides. As oxygen partial pressure increases, oxygen atoms become integrated into the metallic crystal lattice and/or promote the increased formation of sub-oxide phases. This results in gradual amorphization and a transition to electrical insulation. While amorphization occurs, further oxygen incorporation eventually triggers the reformation of crystalline phases, leading to the formation of fully oxidized Y<sub>2</sub>O<sub>3</sub> crystals at room temperature. (AI, AII)
- 2- Yttrium/yttrium oxide thin films produced by magnetron sputtering from a metallic target attain a fully amorphous state characterized by electrical insulation and semi-transparency at an oxygen partial pressure of approximately 7.57×10<sup>-5</sup> P at room temperature. However, when deposition occurs at elevated temperatures around 623 K, it promotes the simultaneous formation of semiconducting yttrium monoxide (YO), which exhibits both cubic and amorphous phases alongside Y<sub>2</sub>O<sub>3</sub>, resulting in an overall semi-transparent material. (AI)
- 3- Photochromic yttrium oxyhydride (YHO) crystallizes into a face-centered cubic (FCC) lattice with the yttrium cations in the oxidation state of ~2.5+ in both bleached and Photodarkened states. (AII, AIII, AIV)
- 4- The Y-Y distance in the face-centered cubic (FCC) lattice of YHO exhibits splitting into two distinct peaks, attributed to both the incorporation of an extra hydrogen atom and the random substitution of hydride anions with oxide anions. This splitting is also influenced by light-induced changes, as the reversible shift of the XRD peak suggests local lattice rearrangements around anion vacancy sites. These vacancies, along with temperature-dependent structural changes, contribute to the observed Y-Y shell splitting and highlight the material's response to UV light exposure through hydrogen diffusion. (AII, AIII, AIV).
- 5- The reason for the photochromism of YHO is related to light absorption by the anion vacancies. The photochromic performance of the YHO thin films can be controlled by adjusting the concentration and/or ratio of anionic defects that can be managed by controlling the residual gas concentration and the H<sub>2</sub>/Ar ratio during the film growth. (AII, AIII, AIV

### **Authors' Patent and Publication List**

#### A. Contributions to the Doctoral Thesis

- 1. **PI** Patent: **Arslan H**., A method for deposition of yttrium monoxide film and yttrium monoxide coatings European Patent EP4033003 (Patent LV / LVP2020000090; LV15646) (**2022**)
- AI- Article: Arslan H., Aulika I., Sarakovskis A., Bikse I., Zubkins M., Azarov A., Gabrusenoks J., Purans J., Reactive pulsed direct current magnetron sputtering deposition of semiconducting yttrium oxide thin film in ultralow oxygen atmosphere: A spectroscopic and structural investigation of growth dynamics, Vacuum, 211 (2023)
- 3. **AII** Article: **Arslan H.**, Kuzmin A., Aulika I, Moldarev D, Wolff M., Primetzhofer D., Pudza I., Kundzins K., Sarakovskis A., Purans J, Karazhanov S. Zh., Chemical state and atomic structure in stoichiovariants photochromic oxidized yttrium hydride thin films, Zeitschrift für Physikalische Chemie, 0 (2024)
- AIII- Article: Arslan H., Pudza I., Kuzmins A., Karazhanov S., Evidence of local structural distortions and subtle thermal disorder in transparent photochromic yttrium oxyhydride, Applied Physics Letters, 124 (2024)
- AIV- Article: Arslan H., Kuzmin A., Kumar K. V., Aulika I., Moldarev D., Primetzhofer D., Wolff M., Pudza I., Nordseth Ø., and Karazhanov S. Zh., Anion Vacancy-Induced Photochromism and Lattice Relaxation in Yttrium Oxyhydride, Submitted manuscript. https://doi.org/10.21203/rs.3.rs-5171857/v1 (2024)

#### **B.** Additional Research Publications

- 1. **BI-** Article: Zubkins M., Aulika I., Strods E., Vibornijs V., Bikse L., Sarakovskis A., Chikvaidze G., Gabrusenoks J., **Arslan H.**, Purans J., Optical properties of oxygen-containing yttrium hydride thin films during and after the deposition, Vacuum, 203 (2022)
- 2. **BII** Article: Zubkins M., **Arslan H.**, Bikse L., Purans J., High power impulse magnetron sputtering of Zn/Al target in an Ar and Ar/O<sub>2</sub> atmosphere: The study of sputtering process and AZO films, Surface and Coatings Technology, 369 (2019)
- 3. **BIII** Article: Skvortsova V., Zubkins M., Kalendarev R., **Arslan H.**, and Purans J., Optical properties of zinc-iridium oxide thin films,

IOP Conference Series: Materials Science and Engineering, 503 (2019)

# **Participation in Conferences**

FM&NT-NIBS (Poster Presentation)

Title: "Reactive E-Beam Evaporation of Yttrium: A Spectral and Structural Analysis of Yttrium Oxide and Oxyhydride Thin Films" (Arslan H., Aulika I., Pudza I., Sarakovskis A., Bikse L., Zubkins M., Chikvaidze G., Purans J.)

University of Latvia, Riga, Latvia | 03.07.2022 – 06.07.2022

E-MRS Virtual Conference (Poster Presentation)

Title: "Reactive E-Beam Evaporation of Yttrium: A Spectral and Structural Investigation of Metallic Yttrium, Yttrium Oxide, and Yttrium Oxyhydride Thin Films"

(Arslan H., Aulika I., Sarakovskis A., Bikse L., Gabrusenoks J., Zubkins M., Purans J.)

30.05.2022 - 03.06.2022

3. Annual ISSP UL Scientific Conference (Poster Presentation) Title: "Reactive E-Beam Evaporation of Yttrium: A Spectral Investigation of Yttrium in Different Chemical Environments" (Arslan H., Aulika I., Sarakovskis A., Bikse L., Gabrusenoks J.,

Chikvaidze G., Zubkins M., Purans J.) Riga, Latvia | 22.02.2022–24.02.2022

E-MRS Virtual Conference (Poster Presentation) Title: "Nanocrystalline-Amorphous Semiconducting Yttrium Monoxide" (Arslan H., Aulika I., Sarakovskis A., Zubkins M., Bikse L., Gabrusenoks J., Purans J.)

20.09.2021 - 23.09.2021

5. Annual ISSP UL Scientific Conference (Oral Presentation) Title: "Deposition and Properties of Yttrium Oxide Thin Films" (Arslan H., Zubkins M., Sarakovskis A., Purans J.) Riga, Latvia | 23.02.2021–25.02.2021

Annual ISSP UL Scientific Conference (Poster Presentation) 6. Title: "Yttrium and Yttrium Oxide Thin Films Deposition by Reactive DC Magnetron Sputtering"

(Arslan H., Zubkins M., Butikova J., Azens A., Butanovs E., Purans J.) Riga, Latvia | 11.02.2020 – 13.02.2020

Advanced Materials and Technologies (Poster Presentation) Title: "Local Structure and Valence State of Iridium in Nanocrystalline and Amorphous Thin Film ZnO-IrO" (Arslan H., Skvortsova V., Zubkins M., Kalendarevs R., Purans J.)

- Palanga, Lithuania | 19.08.2019 23.08.2019
- International Conference on Sputter Technology (Poster Presentation)
   Title: "Y<sub>m</sub>O<sub>n</sub>, Yttrium-Doped ZnO Thin Films and Multilayers"
   (Arslan H., Azens A., Zubkins M., Purans J.)
   Braunschweig, Germany | 19.06.2019 20.06.2019
- 9. E-MRS (Poster Presentation)

Title: "Optical, Structural, and Electrical Characterization of Y doped ZnO Thin Films and Multilayers"

(Arslan H., Azens A., Zubkins M., Purans J.)

Nice, France | 28.05.2019 - 30.05.2019

- 10. Trends in Modern Photon Science (DESY) (Poster Presentation)
  - Title: "Local Structure and Valence State of Iridium in Nanocrystalline and Amorphous Thin Film ZnO-IrO"

(Arslan H., Zubkins M., Gabrusenoks J., Zitolo A., Purans J.)

Hamburg, Germany | 27.02.2019 – 01.03.2019

- 11. Annual ISSP UL Scientific Conference (Poster Presentation)
  - Title: "Optical and Structural Characterization of Y-doped ZnO and  $Y_{n}O_{m}$  Thin Films"

(Arslan H., Zubkins M., Butanovs E., Bikse L., Purans J.)

Riga, Latvia | 20.02.2019 - 22.02.2019

12. FM&NT (Poster Presentation)

Title: "Local Structure and Valence State of Iridium in Nanocrystalline and Amorphous Thin Film ZnO-IrO"

(Arslan H., Zubkins M., Kalendarevs R., Skvortsova V., Purans J.)

Riga, Latvia | 02.10.2018 – 05.10.2018

# **Participation in International Schools**

- International Summer School "Advanced Materials for Chromogenic Device Applications" and "Thin Films: Synthesis and Characterization" Riga, Latvia | 02.06.2024 – 05.06.2024
- 2. Spectroscopy Summer School (Poster Presentation)

Title: "Reactive E-Beam Evaporation of Yttrium: A Spectral and Structural Analysis of Yttrium Oxide and Oxyhydride Thin Films" (Arslan H., Kuzmin A., Pudza I., Sarakovskis A., Purans J., Karazhanov S.)

MAX IV – LINXS, Lund, Sweden | 21.08.2023 – 25.08.2023

# Participation in Large-Scale Research Infrastructure-Based Experiments

- X-ray Absorption Spectroscopy (XAS) Measurement DESY PETRA-III, P65 Hamburg, Germany | 18.04.2024 – 22.04.2024
- X-ray Absorption Spectroscopy (XAS) Measurement DESY PETRA-III, P65 Hamburg, Germany | 11.10.2023 – 16.10.2023
- Rutherford Backscattering Spectrometry (RBS) and Time-of-Flight Elastic Recoil Detection Analysis (TOF-E ERDA) Measurements Tandem Laboratory, Uppsala, Sweden | 08.05.2023 – 11.05.2023

# **Bibliography**

- Singh R., Prakash U., Kumar D. & Laha K. Development of creep resistant high yttria 18Cr ferritic ODS steel through hot powder forging route. Journal of Nuclear Materials, 154566 (2023).
- Fava, S. et al. Magnetic field expulsion in optically driven YBa<sub>2</sub>Cu<sub>3</sub>O<sub>6.48</sub>. Nature, 1-6 (2024).
- Mongstad T. et al. A new thin film photochromic material: Oxygen-containing yttrium hydride. Solar energy materials and solar cells 95, 3596-3599 (2011).
- 4 Kaminaga K. et al. A divalent rare earth oxide semiconductor: Yttrium monoxide. Applied Physics Letters 108 (2016).
- 5 Colombi G., Cornelius S., Longo A. & Dam B. Structure model for anion-disordered photochromic gadolinium oxyhydride thin films. The Journal of Physical Chemistry C 124, 13541-13549 (2020).
- 6 Kumazoe H. et al. Bayesian sparse modeling of extended x-ray absorption fine structure to determine interstitial oxygen positions in yttrium oxyhydride epitaxial thin film. AIP Advances 11 (2021).
- Banerjee S. et al. Exploring Multi-Anion Chemistry in Yttrium Oxyhydrides: Solid-State NMR Studies and DFT Calculations. The Journal of Physical Chemistry C 127(29), 14303-14316 (2023).
- 8 Dam B. et al. Perspective on the photochromic and photoconductive properties of Rare-Earth Oxyhydride thin films. Solar Energy Materials and Solar Cells 273, 112921 (2024).
- 9 Moldarev D., Wolff M. & Primetzhofer D. Modification of the photochromic properties of oxygen-containing yttrium hydride by irradiation with keV and MeV ions. The Journal of Physical Chemistry C 127, 24676-24682 (2023).
- Arslan H. et al. Reactive pulsed direct current magnetron sputtering deposition of semiconducting yttrium oxide thin film in ultralow oxygen atmosphere: A spectroscopic and structural investigation of growth dynamics. Vacuum 211, 111942 (2023).
- Zhang T., Ma S., Xing F. & Zhang L. Diffusivities and atomic mobilities in  $\alpha$ -Y (O) and  $\alpha$ -Y<sub>2</sub>O<sub>3</sub> and their applications to oxidation of pure  $\alpha$ -Y during the initial stage. Solid State Ionics 361, 115559 (2021).
- 12 Djurovic D., Zinkevich M. & Aldinger F. Thermodynamic modeling of the yttriumoxygen system. Calphad 31, 560-566 (2007).
- 13 Yamamoto T., Kaminaga K., Saito D., Oka D. & Fukumura, T. High electron mobility with significant spin-orbit coupling in rock-salt YbO epitaxial thin film. Applied Physics Letters 114 (2019).
- 14 Kaminaga K., Oka D., Hasegawa T. & Fukumura T. New lutetium oxide: Electrically conducting rock-salt LuO epitaxial thin film. ACS omega 3, 12501-12504 (2018).
- Yamamoto T., Kaminaga K., Saito D., Oka D. & Fukumura T. Rock salt structure GdO epitaxial thin film with a high ferromagnetic Curie temperature. Applied Physics Letters 117 (2020).
- Schmehl A. et al. Epitaxial integration of the highly spin-polarized ferromagnetic semiconductor EuO with silicon and GaN. Nature materials 6, 882-887 (2007).
- Sasaki S. et al. A high-TC heavy rare earth monoxide semiconductor TbO with a more than half-filled 4f orbital. Dalton Transactions 51, 16648-16652 (2022).
- Nefedov V., Gati D., Dzhurinskii B., Sergushin N. & Salyn Y. V. X-ray electron study of oxides of elements. Zhumal Neorganicheskoi Khimii 20, 2307-2314 (1975).

- Vasquez R., Foote M. & Hunt B. Reaction of nonaqueous halogen solutions with YBa<sub>2</sub>Cu<sub>3</sub>O<sub>7-x</sub>. Journal of Applied Physics 66, 4866-4877 (1989).
- 20 Hayoz, J. et al. Preparation and characterization of clean, single-crystalline YH $_x$  films (0 $\leqslant$  x $\leqslant$  2.9) on W (110). Journal of Vacuum Science & Technology A: Vacuum, Surfaces, and Films 18, 2417-2431 (2000).
- 21 Greczynski G. & Hultman L. Towards reliable X-ray photoelectron spectroscopy: sputter-damage effects in transition metal borides, carbides, nitrides, and oxides. Applied Surface Science 542, 148599 (2021).
- Mongstad T., Thøgersen A., Subrahmanyam A. & Karazhanov S. The electronic state of thin films of yttrium, yttrium hydrides and yttrium oxide. Solar energy materials and solar cells 128, 270-274 (2014).
- Fujimori A. & Schlapbach, L. Electronic structure of yttrium hydride studied by X-ray photoemission spectroscopy. Journal of Physics C: Solid State Physics 17, 341 (1984).
- 24 Hughes A. & Sexton B. Comments on the use of implanted Ar as a binding energy reference. Journal of electron spectroscopy and related phenomena 50, C15-C18 (1990).
- Pearce S. J., Parker G. J., Charlton M. D. & Wilkinson J. S. Structural and optical properties of yttrium oxide thin films for planar waveguiding applications. Journal of Vacuum Science & Technology A: Vacuum, Surfaces, and Films 28, 1388-1392 (2010).
- Gaboriaud R., Pailloux F., Guerin P. & Paumier F. Yttrium oxide thin films, Y<sub>2</sub>O<sub>3</sub>, grown by ion beam sputtering on Si. Journal of Physics D: Applied Physics 33, 2884 (2000).
- 27 Mudavakkat V., Atuchin V., Kruchinin V., Kayani A. & Ramana C. Structure, morphology and optical properties of nanocrystalline yttrium oxide (Y<sub>2</sub>O<sub>3</sub>) thin films. Optical Materials 34, 893-900 (2012).
- Arslan H. et al. Chemical state and atomic structure in stoichiovariants photochromic oxidized yttrium hydride thin films. Zeitschrift für Physikalische Chemie 0 (2024).
- 29 Sørby M. H., Martinsen F., Karazhanov S. Z., Hauback B. C. & Marstein, E. S. On the Crystal Chemistry of Photochromic Yttrium Oxyhydride. Energies 15, 1903 (2022).
- Hans M. et al. Photochromic mechanism and dual-phase formation in oxygencontaining rare-earth hydride thin films. Advanced Optical Materials 8, 2000822 (2020).
- Mongstad T. et al. Surface oxide on thin films of yttrium hydride studied by neutron reflectometry. Applied Physics Letters 100 (2012).
- Komatsu Y. et al. Repeatable photoinduced insulator-to-metal transition in yttrium oxyhydride epitaxial thin films. Chemistry of Materials 34, 3616-3623 (2022).
- Moldarev D. et al. Composition of photochromic oxygen-containing yttrium hydride films. Solar Energy Materials and Solar Cells 177, 66-69 (2018).
- Powell C. J. Recommended Auger parameters for 42 elemental solids. Journal of Electron Spectroscopy and Related Phenomena 185, 1-3 (2012).
- Majumdar, D. & Chatterjee, D. X-ray photoelectron spectroscopic studies on yttria, zirconia, and yttria-stabilized zirconia. Journal of applied physics 70, 988-992 (1991).
- 36 Baba Y. & Sasaki T. A. Chemical states and thermal stability of hydrogen-implanted Ti and V studied by X-ray photoelectron spectroscopy. Journal of Nuclear Materials 132, 173-180 (1985).
- Mai L. et al. Water assisted atomic layer deposition of yttrium oxide using tris (N, N'-diisopropyl-2-dimethylamido-guanidinato) yttrium (iii): process development, film characterization and functional properties. RSC advances 8, 4987-4994 (2018).

- 38 Kudo Y., Yoshida N., Fujimoto M., Tanaka, K. & Toyoshima I. Acid-dissociation behavior of para-hydroxyl group in the N, N, O-terdentate ligand, 4-(4-methyl-2pyridylazo) resorcinol, coordinated to a transition metal ion. Bulletin of the Chemical Society of Japan 59, 1481-1486 (1986).
- 39 Guo X., Sun Y.-Q. & Cui K. Darkening of zirconia: a problem arising from oxygen sensors in practice. Sensors and Actuators B: Chemical 31, 139-145 (1996).
- 40 Greczynski G. & Hultman L. X-ray photoelectron spectroscopy: towards reliable binding energy referencing. Progress in Materials Science 107, 100591 (2020).
- 41 Aspnes D., Theeten J. & Hottier F. Investigation of effective-medium models of microscopic surface roughness by spectroscopic ellipsometry. Physical Review B 20, 3292 (1979).
- 42 Ordás N. et al. The role of yttrium and titanium during the development of ODS ferritic steels obtained through the STARS route: TEM and XAS study. Journal of Nuclear Materials 504, 8-22 (2018).
- Jonane I. et al. Temperature-dependent EXAFS study of the local structure and lattice dynamics in cubic Y<sub>2</sub>O<sub>3</sub>. Journal of synchrotron radiation 23, 510-518 (2016).
- 44 Bonnet M., Delapalme A. & Fuess H. Redetermination of the scattering length of yttrium. Acta Crystallographica Section A: Crystal Physics, Diffraction, Theoretical and General Crystallography 31, 264-265 (1975).
- 45 Arslan H., Pudza I., Kuzmin A. & Karazhanov S. Evidence of local structural distortions and subtle thermal disorder in transparent photochromic yttrium oxyhydride. Applied Physics Letters 124 (2024).
- Timoshenko J., Kuzmin A. & Purans J. Reverse Monte Carlo modeling of thermal disorder in crystalline materials from EXAFS spectra. Computer Physics Communications 183, 1237-1245 (2012).
- 47 Timoshenko J., Kuzmin A. & Purans J. EXAFS study of hydrogen intercalation into ReO<sub>3</sub> using the evolutionary algorithm. Journal of Physics: Condensed Matter 26, 055401 (2014).
- 48 Arslan H. et al. Anion vacancy-induced photochromism and lattice relaxation in yttrium oxyhydride. Preprint <a href="https://doi.org/10.21203/rs.3.rs-5171857/v1">https://doi.org/10.21203/rs.3.rs-5171857/v1</a> (2024).
- 49 Baba E. M., Montero J., Strugovshchikov E., Zayim E. Ö. & Karazhanov S. Light-induced breathing in photochromic yttrium oxyhydrides. Physical Review Materials 4, 025201 (2020).
- 50 Ramírez R., Tardío M. González R., Chen Y. & Kokta M. R. Photochromism of vacancy-related defects in thermochemically reduced α-Al<sub>2</sub>O<sub>3</sub>:Mg single crystals. Applied Physics Letters 86 (2005).
- Akiyama M., Yamada H. & Sakai K. Photochromism enhancement in reduced tridymite BaMgSiO<sub>4</sub> by Fe-doping. Journal of the Ceramic Society of Japan 119, 338-341(2011).
- 52 Colinet P. et al. The structural origin of the efficient photochromism in natural minerals. Proceedings of the National Academy of Sciences 119, e2202487119, (2022).

## Acknowledgments

Completing my dissertation would not have been possible without the invaluable guidance of my committee members, the unwavering support of my colleagues and friends, and the encouragement of my family.

First and foremost, I express my deepest gratitude to my supervisors, Dr. habil. phys. Juris Purans and Dr. habil. phys. Smagul Karazhanov, for their exceptional guidance, care, and patience. Dr. Purans directed the research on yttrium oxide (YO) with invaluable expertise and support, while Dr. Karazhanov spearheaded the investigation into yttrium oxyhydride (YHO) through his insightful leadership. Their combined efforts fostered an excellent environment for my research throughout my doctoral studies.

I am equally indebted to Dr. phys. Alexei Kuzmins, whose expertise in X-ray Absorption Spectroscopy (XAS) was pivotal to the success of my research. His continuous advice, mentorship, and critical insights have been instrumental throughout my doctoral journey.

Special thanks to Dr. phys. Ilze Aulika, Ph.D. Inga Pudza, Dr. rer. nat. Georgijs Bakradze, Dr. phys. Martins Zubkins, Dr. phys. Jelena Butikova, Dr. Phys. Guna Krieke, and Dr. phys. Boris Polyakov for their assistance, support, and insightful discussions. Additionally, I wish to express my sincere gratitude to my former colleagues at the Institute of Solid State Physics, University of Latvia, as well as the members of the Thin Film and EXAFS Spectroscopy Research Group.

